Journal of Environmental Chemical Engineering 12 (2024) 112418

Contents lists available at ScienceDirect

Journal of Environmental Chemical Engineering

journal homepage: www.elsevier.com/locate/jece

Solar thermo-photocatalytic methanation using a bifunctional RuO_2:TiO_2/Z13X photocatalyst/adsorbent material for efficient CO_2 capture and conversion

Larissa O. Paulista [a,b], Alexandre F.P. Ferreira [a,b], Alírio E. Rodrigues [a,b], Ramiro J. E. Martins [a,b,c], Rui A.R. Boaventura [a,b], Vítor J.P. Vilar [a,b,*], Tânia F.C.V. Silva [a,b,*]

[a] LSRE-LCM - Laboratory of Separation and Reaction Engineering - Laboratory of Catalysis and Materials, Faculty of Engineering, University of Porto, Rua Dr. Roberto Frias, 4200-465 Porto, Portugal
[b] ALiCE - Associate Laboratory in Chemical Engineering, Faculty of Engineering, University of Porto, Rua Dr. Roberto Frias, 4200-465 Porto, Portugal
[c] Superior School of Technology and Management, Bragança Polytechnic University, 5300-253 Bragança, Portugal

ARTICLE INFO

Keywords:
CO_2 capture
CO_2 conversion
Bifunctional photocatalyst/adsorbent material
Thermo-photocatalysis
Solar methane synthesis

ABSTRACT

A novel bifunctional photocatalyst/adsorbent material based on the RuO_2:TiO_2/zeolite 13X (Z13X) composite was developed to enhance solar-driven methanation through simultaneous carbon dioxide (CO_2) capture and thermo-photoconversion. The activity/stability of the hybrid material towards methane (CH_4) production was assessed by varying the (i) photocatalyst composition (Ru load and semiconductor type), (ii) bifunctional material composition (photocatalyst-to-zeolite ratio) and impregnation method, (iii) illumination source and power (simulated sunlight and UVA/Visible LEDs), (iv) temperature, and (v) catalyst reuse. Additionally, adsorption equilibrium isotherms were determined to characterize the adsorption ability of the bifunctional material for both CO_2 and CH_4 gases. The hybrid $RuO_{2(4.0\%)}$:$TiO_{2(26.3\%)}$/Z13X material (30 mg), synthesised by the solid-state impregnation method, showed the best results under simulated sunlight (0.75 W) at 150 ºC, achieving a 88% CO_2 thermo-photoreduction after 100 min, corresponding to a specific CH_4 production of 29.2 mmol $g^{-1}_{active\_cat}$ h^{-1} (309 mmol g^{-1}_{Ru} h^{-1}) and apparent quantum yield of 20.7%. In adsorption equilibrium isotherms, the bifunctional material's adsorption was about 2.6-fold higher than the photocatalyst at 150 ºC, suggesting that enhanced methanation performance can be attributed to the synergistic action of CO_2 capture and thermo-photoconversion.

1. Introduction

The escalating release of CO_2 into the atmosphere due to human activities, such as fuel combustion, industrial processes, and gas processing, has intensified anthropogenic concentrations of greenhouse gases and climate change concerns. To tackle this global issue and achieve carbon neutrality, humanity will inevitably confront profound challenges in the foreseeable future [1]. A viable strategy may involve developing a carbon cycle-based approach for capturing and transforming CO_2 into sustainable fuels that can be further used in the production chain [2]. While previous efforts have focused on converting CO_2 into specific chemicals, such as dimethyl carbonates, cyclic carbonates, and polycarbonates, the market demand for these products can limit their widespread implementation. Consequently, there is a growing interest in CO_2 conversion into chemical feedstocks and fuels, such as CO_2 hydrogenation, Fischer-Tropsch synthesis, and bio-reforming processes [3]. One promising pathway to mitigate CO_2 emissions and advance sustainable fuel production, which has attracted considerable research interest, is the solar-driven photocatalysis-based methanation technology, where CO_2 and hydrogen (H_2) are converted to CH_4 (Sabatier reaction) to produce synthetic natural gas. In this sense, nanomaterials are being explored to capture and directly convert CO_2 into valuable chemicals, offering a more environmentally friendly and efficient approach under mild reaction conditions [4].

Recent developments in nanoscience and nanotechnology have opened up new possibilities for efficient CO_2 recycling despite the

* Corresponding authors at: LSRE-LCM - Laboratory of Separation and Reaction Engineering - Laboratory of Catalysis and Materials, Faculty of Engineering, University of Porto, Rua Dr. Roberto Frias, 4200-465 Porto, Portugal.
E-mail addresses: vilar@fe.up.pt (V.J.P. Vilar), tania.silva@fe.up.pt (T.F.C.V. Silva).

https://doi.org/10.1016/j.jece.2024.112418
Received 15 November 2023; Received in revised form 19 February 2024; Accepted 5 March 2024
Available online 8 March 2024

challenges posed by the complexity of CO_2 reduction and the intrinsic difficulty in creating efficient single-component photocatalysts. Several enhancement mechanisms have been identified regarding the generation of charge carriers (electron-hole pairs), their separation and transfer to the photocatalyst surface, and chemical reactions between surface species and photogenerated electron-holes [5]. Doping a semiconductor with metal or non-metal molecules can significantly enhance the light absorption of a photocatalyst by modifying its electronic structure [6]. Another approach to improve photocatalyst efficiency involves combining semiconductor photocatalysts with reduction and oxidation cocatalysts. Additionally, bioinspired techniques, such as Z-scheme heterojunction and alternative Z-scheme systems, are being explored for their potential to enhance photocatalytic performance [7]. Developing bifunctional materials through the strategic integration of photocatalysts within porous CO_2 adsorbent materials, such as metal-organic frameworks (MOFs) and zeolites [4,8,9], is another promising approach that can improve CO_2 reduction by organizing light-harvesting and catalytic centres. Materials should have robust adsorption capacity, selectivity, low toxicity, and the ability to withstand extreme conditions. The adsorption capacity of these materials can be increased by altering their surfaces by grafting, impregnation, or functionalization, thereby boosting their CO_2 capture and photocatalytic conversion capabilities [4].

Titanium oxide (TiO_2)-based materials have been widely used as semiconductors for photocatalytic CO_2 reduction due to their non-toxicity, affordability, stability, resistance to photo-corrosion, and abundance [10]. Another potential semiconductor for this application is strontium titanate ($SrTiO_3$), known for its cost-effectiveness, safety, and high thermal and photochemical stability [11]. Furthermore, ruthenium (Ru)-based catalysts can enhance photocatalytic CO_2 conversion by promoting efficient H_2 dissociation and CO_2 methanation at low temperatures, improving visible-light absorption and facilitating photo-generated charge transfer [12]. Building upon this finding, CO_2 reduction via thermo-photocatalysis achieved a conversion rate of 93.8% at 220 ºC, using a photocatalyst based on Ru-metal doped TiO_2 under Xe lamp illumination [13]. A similar performance was reported by Mateo et al. [14], where a 90% CO_2 conversion was accomplished after a 2-hour reaction at 150 ºC utilizing a $RuO_2/SrTiO_3$ catalyst inspired in a Ru-oxide state strategy under Xe lamp irradiation.

As one of the best commercial adsorbents for carbon capture, zeolite 13X (USY type) can be functionalized with catalysts to improve conversion yields by attracting CO_2 to the catalyst's active sites [15]. Integrating porous and catalytic materials can be a promising approach for CO_2 capture and conversion, taking advantage of its unique features such as size, shape, porosity, and catalytically active centres. Consequently, there is potential for meaningful research focusing on materials that can adsorb CO_2 and rapidly release the reaction products for efficient conversion processes [4]. Moreover, heterogenous thermo-photocatalysis, an emerging hybrid process that combines the benefits of both photocatalysis and thermal catalysis, can be employed to attain high CO_2 conversions under mild conditions [16]. While previous research has explored zeolite-supported catalytic materials for CO_2 conversion into CH_4 via thermo-catalytic hydrogenation, typically conducted at high temperatures (> 250 ºC) with high reaction rates, as well as through water-mediated heterogeneous photocatalysis, which operates at room temperature but with comparatively lower efficiencies (on the order of μmol g^{-1} h^{-1}), there is still a critical need for further investigation [9,17]. To the best of our knowledge, the application of these materials to promote efficient CO_2 thermo-photocatalytic methanation under moderate reaction conditions is unprecedented in the existing literature.

Therefore, this study aimed to explore, for the first time, the potential of a novel bifunctional material consisting of a zeolite 13X adsorbent impregnated with a RuO_2-loaded TiO_2 photocatalyst to foster simultaneous adsorption and thermo-photocatalytic hydrogenation of CO_2 into sustainable CH_4 at low temperatures. The investigation was conducted under gas-phase and batch operation mode using sunlight as a renewable energy source. The photoactivity was assessed concerning material composition and dosage, illumination source, temperature, and material reusability towards highly efficient CO_2-to-CH_4 conversion. Moreover, the study evaluated the adsorption ability of the bifunctional photocatalyst/adsorbent composite and the apparent photonic efficiency to gain a comprehensive understanding of the overall reaction.

2. Materials and methods

2.1. Chemical products

Table S2 provides a concise overview of all chemical compounds employed during the different experimental procedures. All the chemicals were used as received without any further purification. The photocatalytic materials were prepared and rinsed with ultrapure water (UPW) produced by a Millipore Direct-Q® system, featuring a resistivity of 18.2 MΩ cm^{-1} at 25 °C.

2.2. Synthesis of the hybrid bifunctional material

Initially, the RuO_2-loaded photocatalyst powder was synthesized through ethylene glycol reduction by adapting the experimental procedure reported in previous work (Fig. 1a) [18,19]. Briefly, TiO_2 or $SrTiO_3$ was immersed in ethylene glycol (5 mg mL^{-1}, 25 mL), along with different amounts of $RuCl_3{\cdot}H_2O$, to achieve [Ru]:[TiO_2] or [Ru]:[$SrTiO_3$] mass ratios of 1:10, 2:10, and 3:10. Then, this solution underwent: (i) sonication (Vibra Cell™ VCX 130, Sonics, Newtown, USA) for 30 min at 20 kHz (80% amplitude with pulse 1-on 2-off); (ii) heating for 5 h at 100 ºC (to improve Ru fixation into the semiconductor) under continuous stirring; and (iii) refluxing for 8 h at 180 ºC under continuous stirring. The resulting material was filtered (Nylon membrane filter, 0.22 μm, Ø 47 mm) and washed with UPW (1 L) and acetone (200 mL), followed by drying for 1 h at 100 °C and calcination for 3 h at 350 °C (Fig. 1a).

Afterwards, the optimised photocatalyst (before being subjected to calcination) was incorporated into the zeolite 13X adsorbent using either the wet impregnation method (WIM, Fig. 1b.1) or solid-state impregnation method (SIM, Fig. 1b.2), with [RuO_2:TiO_2]:[Z13X] mass ratios of 1:10, 2:10, 3:10, and 4:10 or 2:10, 3:10, 4:10, and 5:10, respectively. The WIM consisted of the following steps: (i) dispersion of 200 mg of zeolite 13X in 10 mL of UPW by sonication for 15 min; (ii) slow evaporation at 70 ºC under stirring while gradually adding 5 mL of UPW containing the desired photocatalyst amount; and (iii) drying for 1 h at 100 °C. The SIM comprised the following steps: (i) manual mixing of the zeolite 13X with the photocatalyst for 15 min using a pestle and agate mortar; and (ii) mechanical mixing/grinding for 30 min using an RM100 Laboratory Mixer-Mortar-Grinder. The bifunctional materials (RuO_2:TiO_2/Z13X or RuO_2:$SrTiO_3$/Z13X - only for the best mass ratio prepared by SIM) resulting from both WIM and SIM were calcinated for 3 h at 350 °C.

The content of Ru metal in the photocatalyst was determined by inductively coupled plasma emission spectrometry (ICP-OES) after proper extraction by microwave digestion technique (heating rate of 11 °C min^{-1}; temperature of 220 °C for 40 min). The estimated materials composition is presented in Table S2. The digestion process was employed on the photocatalytic material before it passed through calcination. It used an acid mixture of aqua regia fortified with hydrogen peroxide (see Table S3) to enhance extraction efficiency. The extraction of the Ru metal from the catalyst was considered complete when no dark powder was found in the resulting digested solution, as displayed in Figure S1(b). It should be noted that metal extraction from a material can be challenging, particularly after the calcination process [20], and using aqua regia solution alone can be inadequate, resulting in underestimated metal content. Therefore, providing information on the amount of metal added during the photocatalyst preparation process is

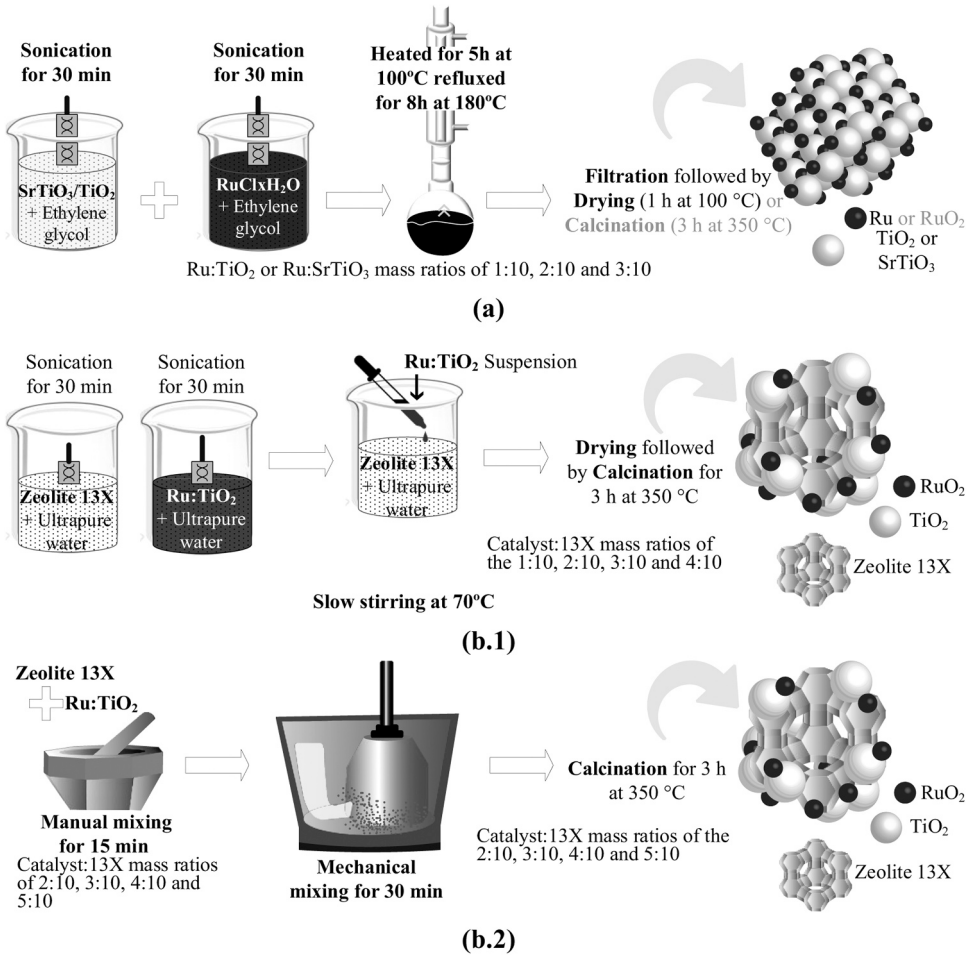

Fig. 1. Experimental methodology for the preparation of the bifunctional photocatalyst/adsorbent composite: (a) synthesis of RuO_2:TiO_2 and RuO_2:$SrTiO_3$ photocatalysts; (b) impregnation of the photocatalyst into the zeolite 13X absorbent using (b.1) wet and (b.2) solid-state impregnation methods (WIM and SIM).

essential so the readers can replicate it.

2.3. Materials characterisation techniques

A detailed description of the analytical methods used to characterise the synthesised materials can be found in Table S3.

2.4. Experimental procedure

2.4.1. Thermo-photocatalytic CO_2 methanation experiments

The thermo-photocatalytic hydrogenation of CO_2 into CH_4 was assessed in a batch-mode laboratory unit (Figure S2a). The experimental facility consisted of a 40 mL gas-phase quartz cylindrical reactor connected to temperature (up to 300 ºC) and pressure (up to 4 bar) control systems. Two light sources were used to illuminate the quartz reactor: (i) a sunlight simulator (Atlas, Suntest XLS+, Linsengericht, Germany), emitting polychromatic radiation within 280–800 by a Xenon lamp; or (ii) a monochromatic light emitting diode (LED) (Lightningcure, LC-L1, V5, Hamamatsu) of 365 nm (UVA) or 405 nm (visible). The radiant power (RP)/photon flux (Pa) reaching inside the reactor was determined for each irradiation source by ferrioxalate actinometry as described in Supplementary Material. A digital infrared thermometer (UNIT-T, UT300S) was used to verify the reactor's internal temperature. Gas samples were directly withdrawn from the reactor headspace to an *on-line* gas chromatography (GC) analytical system (YL 6500, YL Instrument CO. LTD, Anyang, Korea) via a peristaltic pump. The reactants (CO_2 and H_2) and products (CH_4 and C_2H_6) were quantified by a GC analytical system equipped with a: (i) Carbon Plot column (30 m × 0.32 mm × 3.0 μm, Agilent Technologies, California, USA) followed by a Mol Sieve 5 A Plot fused silica capillary column (30 m × 0.32 mm × 3.0 μm, Supelco, Missouri, USA); and (ii) micro-thermal conductivity detector (μTCD) (sensitivity of 400 pg mL^{-1}) followed by methaniser (to convert CO_2 into CH_4) and a flame ionization detector (FID) (sensitivity of 1.5 pg carbon sec^{-1}). Within the system are two six-way valves: (i) the primary injecting valve (placed before the first column), which regulates the injection of the gas sample through the sampling loop, enabling real-time product analysis; and (ii) the secondary switching valve (placed between the two columns), which acts as a safety mechanism for the Molsieve 5 Å column, preventing the passage of excessive concentrations of CO_2 and C_{2+} elements through it [21].

The experimental protocol regarding the methanation tests involved the following steps: (i) dispersion of the powder catalytic material (20, 30, 40, or 60 mg of RuO_2:TiO_2, RuO_2:$SrTiO_3$, RuO_2:TiO_2/Z13X or RuO_2:$SrTiO_3$/Z13X) at the bottom of the quartz photoreactor, followed by a 10-min purging with H_2; (ii) feeding with a gas mixture containing the stoichiometric [CO_2]:[H_2] molar ratio (1:4) up to a total pressure of 1.6 bar (P_{CO2}:P_{H2} (bar/bar) of 0.32:1.28) and collection of the first control sample (t = 0 min); (iii) activation of the heating system (50, 100, 150, 200, or 250 ºC) and collection of the second control sample (t = 10 min); (iv) switching on the illumination source (with RP values of 0.420 ± 0.008, 0.60 ± 0.01, 0.75 ± 0.01 or 1.090 ± 0.03 W, for Xe lamp; 0.055 ± 0.008; 0.30 ± 0.07, and 0.55 ± 0.07 W, for 405 nm LED; or 0.055 ± 0.009; 0.30 ± 0.05, and 0.55 ± 0.08 W, for 365 nm LED) to start the reaction; and (v) collection of five additional samples until 100 min reaction period (t = 20, 30, 50, 70 and 100 min). At the end of the reaction, the photoreactor was cooled, cleaned with a compressed

air jet, rinsed with UPW, and dried for 3 h at 100 °C.

2.4.2. Adsorption equilibrium isotherms

The adsorption equilibrium isotherms of CO_2 and CH_4 in Z13X, RuO_2:TiO_2, and RuO_2:TiO_2/Z13X samples were determined at 150, 200, and 250 °C (pressure up to 5 bar) using a magnetic suspension microbalance (MSB, Rubotherm, precision of 0.01 mg, Figure S2b). Before conducting the adsorption equilibrium measurements, the samples were subjected to an activation step for 24 h at 300 °C under vacuum. Then, the gas was gradually introduced into the gas cell containing the material until the selected pressure was reached. The pressure was maintained until the mass difference approached zero, indicating equilibrium. After that, the gas was slowly added to achieve subsequent pressure levels, corresponding to additional points on the adsorption equilibrium isotherm. This process was repeated up to a maximum pressure of 5 bar. The desorption points were obtained by depressurising the gas cell. After each measurement, the material was regenerated under a vacuum for 24 h at 300 °C.

2.5. Calculation formulas

The Supplementary Material file provides all the calculation formulas used to assess the CO_2 conversion efficiency, including the determination of pseudo-first-order kinetic parameters, the apparent photonic efficiency, quantum yield and activation energy, as well as the adsorption equilibrium isotherms.

3. Results and discussion

3.1. Material characterisation

Thermo-photocatalytic CO_2 hydrogenation reactions were mainly carried out over a new hybrid bifunctional material consisting of the zeolite 13X (Z13X) adsorbent impregnated with a RuO_2-loaded TiO_2 photocatalyst, according to the procedure previously described in Section 2.2 and Fig. 1. The materials composition (in wt%) was estimated by ICP-OES analysis, and it is reported with the following general notation: $RuO_{2(\%)}$:$TiO_{2(\%)}$/Z13X (Table S2). Besides, to understand the structural, physical, and morphological changes in the bifunctional

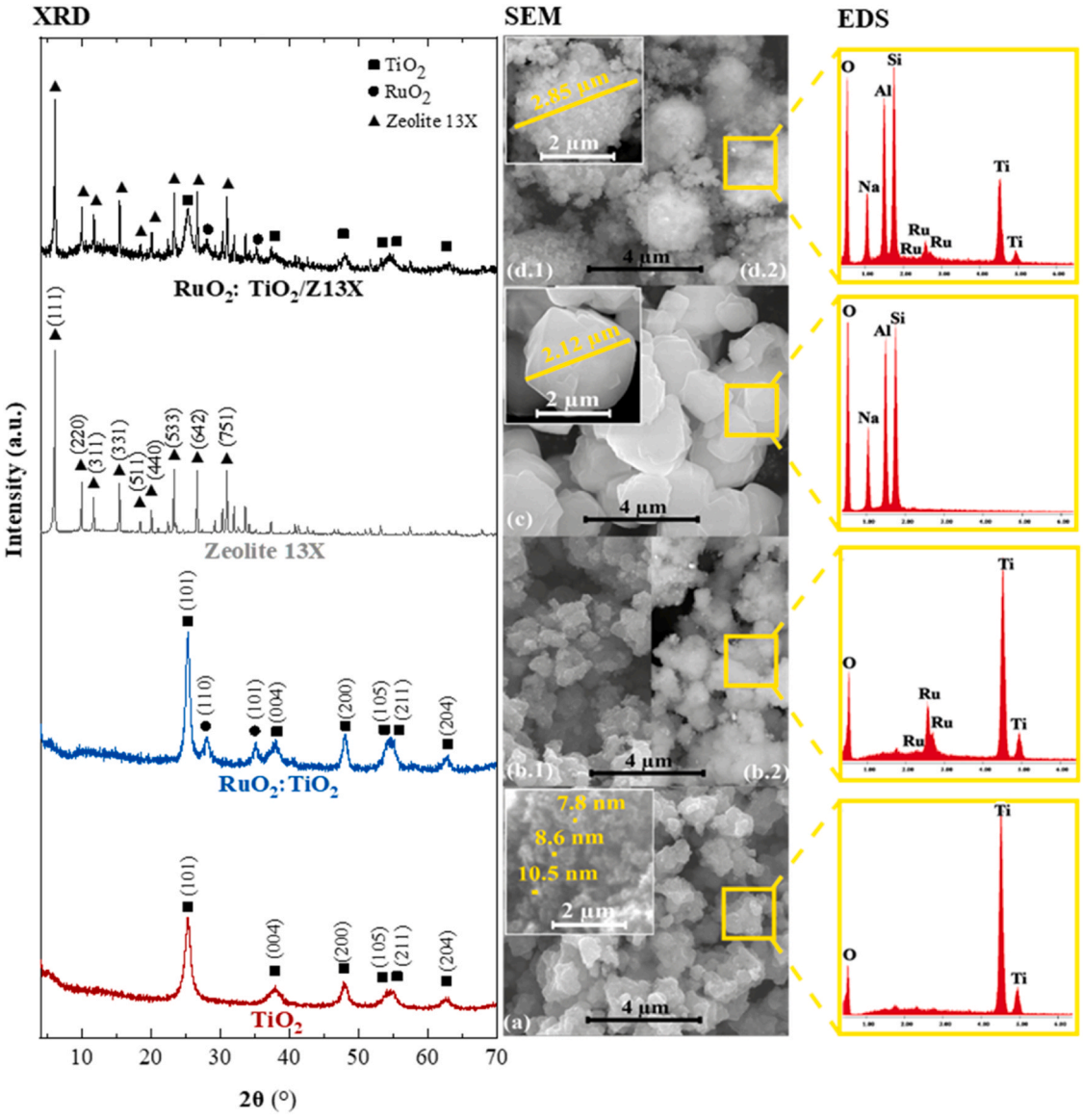

Fig. 2. XRD patterns and SEM/EDS images/spectra for (a) TiO_2, (b) $RuO_{2(13.4\%)}$:TiO_2, (c) zeolite 13X, and (d) $RuO_{2(4.0\%)}$:$TiO_{2(26.3\%)}$/Z13X. SEM micrographs were captured using (a, b.1, c, d.1) secondary electrons (SEs) and (b.2, d.2) backscattered electrons (BSEs).

composite, pristine TiO_2 and Z13X, and $RuO_{2(13.4\%)}$:TiO_2 and $RuO_{2(4.0\%)}$:$TiO_{2(26.3\%)}$/Z13X materials were characterised by several techniques (Table S3), including: (i) X-ray Powder Diffraction (XRD); (ii) Scanning Electron Microscope/Energy-dispersive X-ray Spectroscopy (SEM/EDS); (iii) UV-Vis Diffuse Reflectance Spectroscopy (DRS); (iv) Fourier Transform Infrared Spectrophotometry (FTIR); (v) High-Resolution X-Ray Photoelectron Spectroscopy (XPS); and (vi) He picnometry, CO_2 adsorption at 273 K, and N_2 adsorption at 77 K.

3.1.1. XRD pattern

The XRD pattern in Fig. 2 illustrates the crystalline structure of TiO_2, $RuO_{2(13.4\%)}$:TiO_2, Z13X, and $RuO_{2(4.0\%)}$:$TiO_{2(26.3\%)}$/Z13X materials. Pure TiO_2 exhibits characteristic diffraction peaks of the anatase phase with a tetragonal crystal system (a = 3.7971 Å and c = 9.5790 Å), in agreement with commercial information and reference [22]. The XRD peaks were observed at 25.3°, 37.9°, 47.8°, 54.0°, 55.0°, and 62.6°, corresponding to the (101), (004), (200), (105), (211), and (204) crystal planes of the anatase phase in TiO_2, respectively [23]. As expected, no diffraction peaks associated with the rutile phase were observed, indicating an exclusive anatase phase in the sample. In $RuO_{2(13.4\%)}$:TiO_2, the anatase crystal structure of commercial TiO_2 has been preserved, with the addition of peaks at 27.9° and 35.1°, corresponding to the (110) and (101) crystal planes of the tetragonal crystal system from RuO_2 [24]. The XRD pattern of pure zeolite 13X was in agreement with the commercial information, showing typical diffraction peaks at 6.1°, 9.9°, 11.7°, 15.4°, 18.4°, 20.0°, 23.2°, 26.6°, and 30.9°, which corresponds to (111), (220), (311), (331), (511), (440), (533), (642), and (751) crystal planes of the zeolite 13X [25]. The XRD pattern of the $RuO_{2(4.0\%)}$:$TiO_{2(26.3\%)}$/Z13X bifunctional material showed diffraction peaks comparable to those of pristine zeolite 13X, indicating that the structural framework of the adsorbent was preserved, even after photocatalyst impregnation. Additionally, distinctive peaks associated with both TiO_2 in the anatase phase and the crystal structure of RuO_2 were observed in the bifunctional material, further confirming the presence and preservation of the catalyst within the material.

3.1.2. Morphology and physical characterisation

The materials used in this work were morphologically characterised by SEM/EDS analysis (Fig. 2). SEM image of TiO_2 shows spherical particle clusters with sizes around 7.8–10.5 nm, representing the elemental composition of Ti and O (as stated in EDS), confirming the specifications of the TiO_2 CristalACTiV™ PC-500 powder (Fig. 2a). As regards the $RuO_{2(13.4\%)}$:TiO_2 photocatalyst (Fig. 2b), SEM images were captured using secondary electrons (SEs) and backscattered electrons (BSEs), each offering different types of information. Although SE images offer a higher level of surface detail, BSE images are sensitive to atomic number variations, resulting in brighter areas representing materials with higher atomic numbers [26]. Therefore, Fig. 2b.1 depicts the morphology of the doped photocatalyst, which is very similar to that of pristine TiO_2, as expected. On the other hand, due to its higher atomic number, Fig. 2b.2 highlights the presence of the brighter Ru particles, uniformly distributed within the TiO_2 matrix.

As shown in Fig. 2c, zeolite 13X material has a crystalline octahedral cuboid morphology [27] with a particle size between 1.46 and 2.12 μm and is composed of Na, Al, and Si elements, in agreement with the commercial specifications for zeolite 13X NaMSX P-TR. The bifunctional $RuO_{2(4.0\%)}$:$TiO_{2(26.3\%)}$/Z13X material (Fig. 2d) featured a sphere size of approximately 2.85 μm consisting of Ti, Ru, Na, Al, and Si, with a catalyst layer thickness estimated in 0.36 μm. The SEM-BSEs images (Fig. 2d.2) reveal a uniform distribution of Ru particles. As almost no

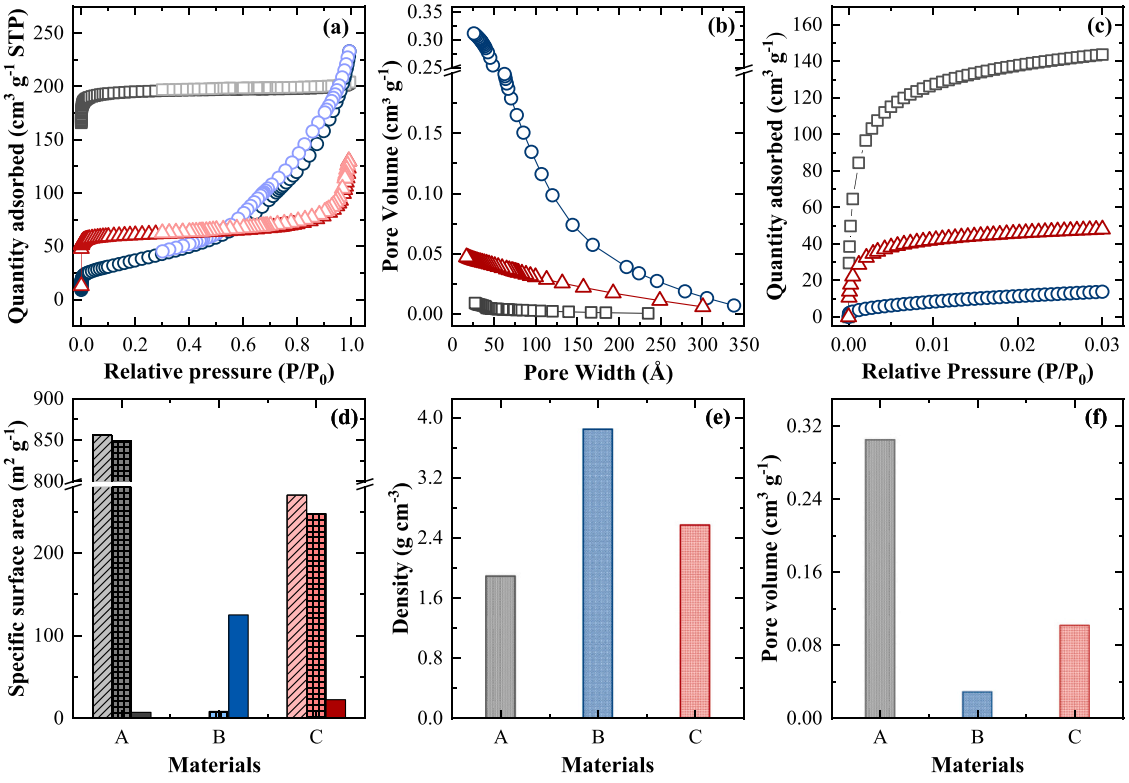

Fig. 3. Physical characterisation of zeolite 13X (□, A), $RuO_{2(13.4\%)}$:TiO_2 (◯, B), and $RuO_{2(4.0\%)}$:$TiO_{2(26.3\%)}$/Z13X (△, C) materials, including: **(a)** N_2 adsorption–desorption isotherms at standard temperature and pressure (STP); **(b)** pore volume *vs.* pore width; **(c)** CO_2 adsorbed as a function of relative pressure; **(d)** specific surface area: Langmuir surface area (▨), t-plot micropore area (▩), and t-plot external surface area (■); **(e)** density; and **(f)** total pore volume, considering pores less than 7.968 Å width at P/P_0 = 0.03.

large-sized Ru particle aglomerates were found on the catalyst surface, zeolite's porous nature and supporting function were successfully demonstrated by the uniform distribution of catalyst particles all over the bifunctional material (Fig. 2d.1).

The physical characterisation of the pristine zeolite 13X, $RuO_{2(13.4\%)}$:TiO_2, and $RuO_{2(4.0\%)}$:$TiO_{2(26.3\%)}$/Z13X materials is presented in Table S4 and Fig. 3. Fig. 3a depicts the N_2 adsorption-desorption isotherms. The adsorption-desorption profile of commercial zeolite 13X exhibits a typical type-I isotherm (IUPAC classification) ascribed to microporous adsorbent materials [28]. Conversely, the $RuO_{2(13.4\%)}$:TiO_2 catalytic material displays a type II physisorption isotherm, usually assigned to nonporous or macroporous materials [29]. The hybrid $RuO_{2(4.0\%)}$:$TiO_{2(26.3\%)}$/Z13X material demonstrates a behaviour similar to zeolite 13X, albeit with a lower adsorption capacity than the zeolitic material. This performance suggests that in the hybrid material obtained through physical impregnation, the surface of zeolite 13X is likely covered by a catalytic material coating, which hinders N_2 adsorption at a low temperature of 77 K, besides the mass dilution effect due to the catalyst impregnation [28]. Indeed, the hybrid material, $RuO_{2(4.0\%)}$:$TiO_{2(26.3\%)}$/Z13X, is primarily composed of zeolite 13X, which features a concentration of 70 wt%. Yet, its surface area and pore volume did not exhibit a direct proportionality concerning the zeolite 13X amount. In fact, N_2 adsorption measurements indicate that the surface area and pore volume of the catalyst/Z13X composite corresponds to roughly 30% of the zeolite 13X one. One possible explanation for this observation is the physical obstruction of zeolite pores [30] by the catalytic material layer. The catalyst layer has an approximate thickness of 0.36 μm, as evidenced by SEM images, and is formed around the zeolite 13X. The pore volume ($cm^3\ g^{-1}$) per pore width (Å) measured by N_2 adsorption at 77 K further supports this effect (Fig. 3b). Although there is physical obstruction of the zeolite pores, which reduces its ability to adsorb CO_2, the hybrid material still features a 4-fold higher adsorption capacity than the catalytic material (Fig. 3c).

The Langmuir surface area, micropore area, and external surface area (Fig. 3d) were, respectively: 856.0, 848.8, and 7.3 for zeolite 13X; and 270.2, 247.6, and 22.6 $m^2\ g^{-1}$ for $RuO_{2(4.0\%)}$:$TiO_{2(26.3\%)}$/Z13X. The hybrid material presents a three times smaller Langmuir's surface area and micropore area, along with the opposite outcome in the external surface area, confirming the presence of a catalyst on the zeolite's surface. The density of the hybrid $RuO_{2(4.0\%)}$:$TiO_{2(26.3\%)}$/Z13X was estimated to be 2.56 g cm^{-3} (Fig. 3e) by helium pycnometry, which is directly proportional to the material composition. The total pore volume, considering pores less than 7.968 Å width at $P/P_o = 0.03$ (Fig. 3e), estimated by CO_2 adsorption at 273 K, is 0.30, 0.03, and 0.10 $cm^3\ g^{-1}$ for the zeolite 13X, catalyst, and bifunctional material, respectively. Furthermore, the percentage of pore volume featuring less than 8.04 Å width in total volume (Table S4) are 96%, 4%, and 64% for zeolite 13X, $RuO_{2(13.4\%)}$:TiO_2, and $RuO_{2(4.0\%)}$:$TiO_{2(26.3\%)}$/Z13X, respectively. The highest microporosity value is typical of microporous materials such as zeolite 13X [31]. In a hybrid material, retaining the individual characteristics of each isolated material is difficult. Nevertheless, the notable increase in its microporosity (~60%) compared to the catalytic material can improve the performance of CO_2 conversion, as further explored.

3.1.3. UV–vis diffuse reflectance spectra

By analysing the DRS results (Fig. 4a) and employing the Tauc plot method to estimate the optical band gap energy (E_g), it was possible to determine the maximum light wavelength (λ_{max}) at which electron excitation occurs within each material (Fig. 4b). As expected, zeolite 13X showed almost no absorption ability across the 280–800 nm wavelength range. Commercial TiO_2 demonstrated high absorption in the UVA region (Fig. 4a), rendering in an E_g of 3.33 eV and a λ_{max} of 373 nm (Fig. 4b.1). Conversely, a remarkable enhancement in the radiation absorption capacity was observed when the TiO_2 was loaded with RuO_2 ($RuO_{2(13.4\%)}$:TiO_2), especially in the visible range, which implies a decrease in E_g of approximately 50% (1.65 eV) and an increase in λ_{max} up to 753 nm (Fig. 4b.2). Some studies have demonstrated that incorporating RuO_2 in semiconductors increases the efficiency of visible-light-driven processes, attributing this effect to surface plasmon resonance of Ru-oxide, which exhibits a high visible light absorption [14, 18]. According to Linic et al. [32], these photo-excited plasmonic nanostructures exhibit relatively high photocatalytic activity when

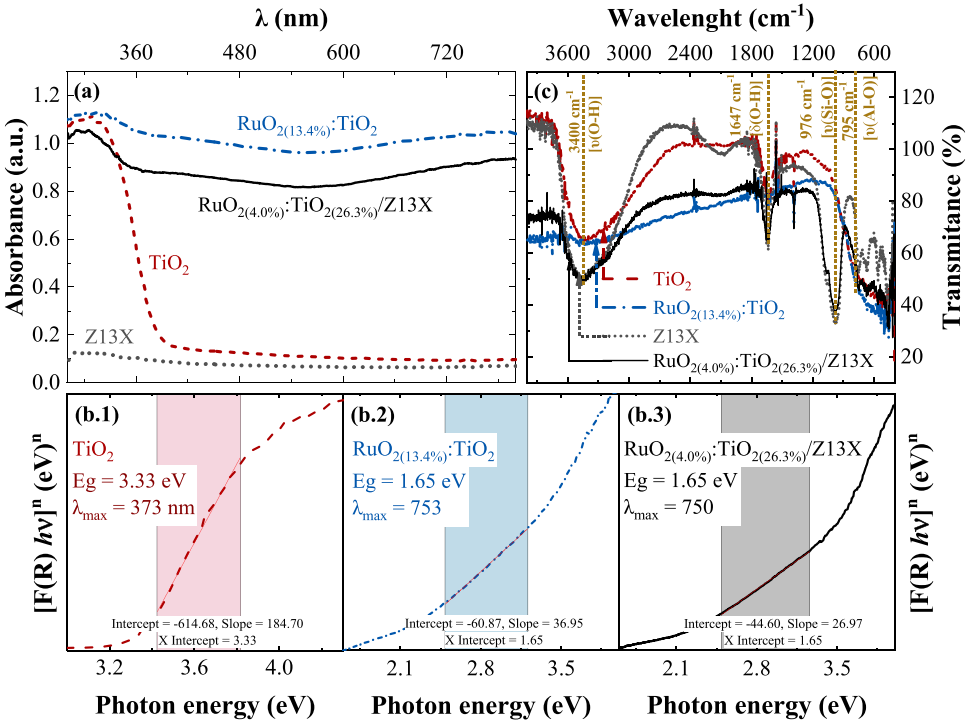

Fig. 4. Representation of (a) UV–vis DRS data, (b) optical band gap energy (*Eg*) determination (according to Tauc Plot method), and (c) FTIR spectra for zeolite 13X (dotted line), (.1) TiO_2 (dashed line), (.2) $RuO_{2(13.4\%)}$:TiO_2 (dotted-dashed line), and (.3) $RuO_{2(4.0\%)}$:$TiO_{2(26.3\%)}$/Z13X (solid line) materials.

exposed to resonant photons from light sources with intensities comparable to those of sunlight. Fig. 4a reveals a minor decrease in absorbance when the zeolite 13X is functionalised with the catalytic material. The narrow difference between $RuO_{2(13.4\%)}$:TiO_2 and $RuO_{2(4.0\%)}$:$TiO_{2(26.3\%)}$/Z13X materials confirms an effective impregnation process, where the catalytic material adequately envelops the adsorbent material, not leaving its surface exposed, as evidenced by SEM images. This observation is further supported by the consistent band gap value of 1.65 for both materials, as depicted in Fig. 2b.2 and b.3.

3.1.4. FTIR spectroscopy

Fig. 4c depicts the FTIR spectra of pristine TiO_2 and zeolite 13X materials, as well as $RuO_{2(13.4\%)}$:TiO_2 and $RuO_{2(4.0\%)}$:$TiO_{2(26.3\%)}$/Z13X composites. In agreement with the XRD pattern (Fig. 2a), commercial TiO_2 PC500 displays a wideband between 400 and 800 cm^{-1}, typical of the anatase phase [33]. In the $RuO_{2(13.4\%)}$:TiO_2 catalyst, additional bands were observed at 690 cm^{-1} and 871 cm^{-1}, corresponding to υ(Ru-O-Ru)/υ(Ru-O-Ti) and υ(Ru-O) vibrations, respectively [33]. Zeolite 13X shows typical bands at 795 cm^{-1} and 976 cm^{-1}, which can be assigned to υ(Al-O) and υ(Si-O) stretching vibrations [34]. The resulting bifunctional material exhibits spectral bands that align with the catalyst composition (RuO_2 and TiO_2) while preserving the characteristic zeolite 13X bands without any detectable impurities.

3.1.5. High-resolution XPS spectra

XPS analysis (Fig. 5) confirmed the elemental/chemical surface

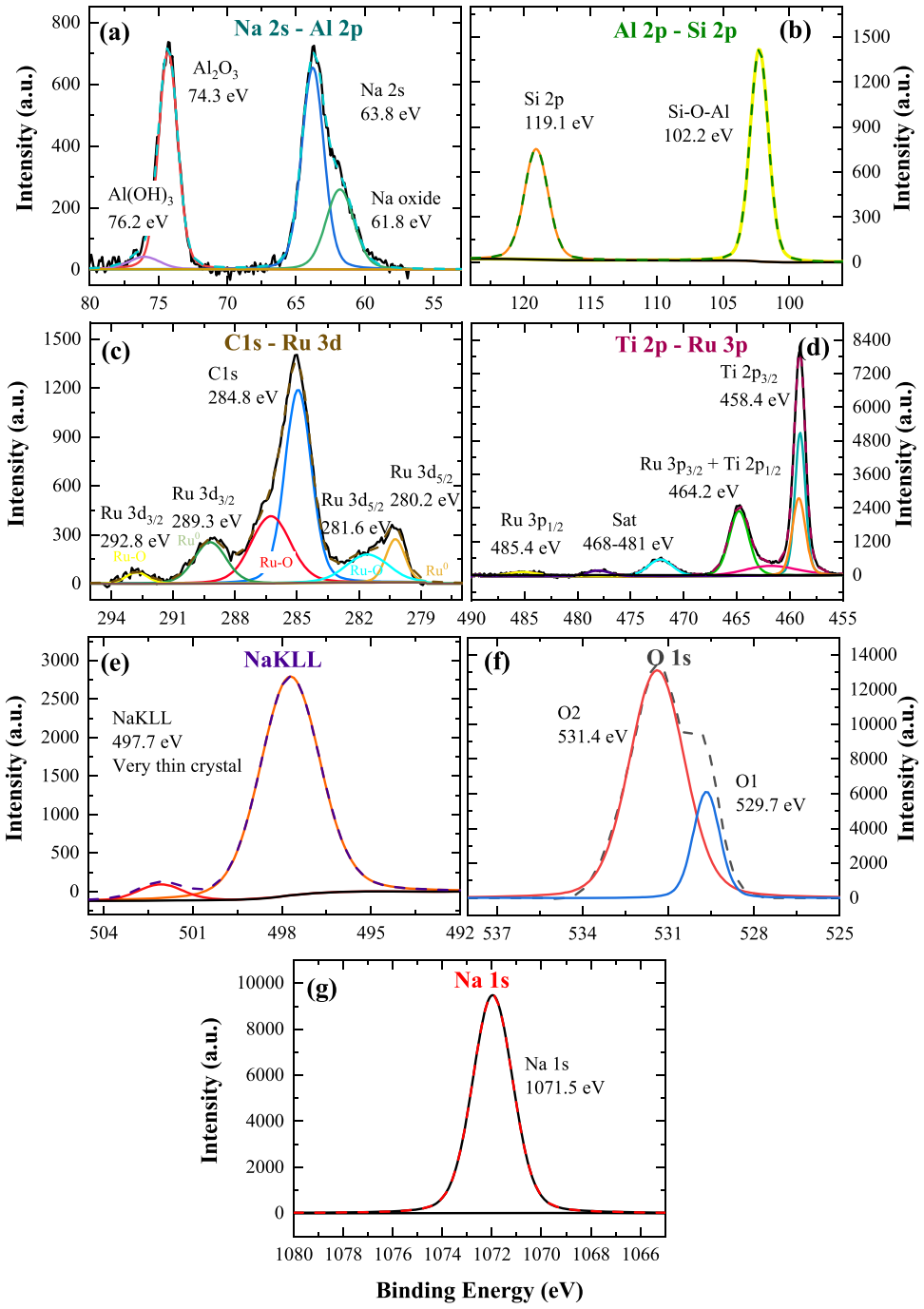

Fig. 5. High-resolution XPS spectra of **(a)** Na 2 s – Al 2p, **(b)** Al 2p – Si 2p, **(c)** C1s – Ru 3d, **(d)** Ti 2p – Ru 3p, **(e)** NaKLL, **(f)** O 1 s, and **(g)** Na 1 s occupied states with the respective fitting and deconvolution curves for the $RuO_{2(4.0\%)}$:$TiO_{2(26.3\%)}$/Z13X bifunctional material.

composition of the fresh hybrid $RuO_{2(4.0\%)}$:$TiO_{2(26.3\%)}$/Z13X material, which includes Ru, Ti, Al, Na, Si, and O components, without the presence of impurities. The surface charge effect was corrected, considering that the lowest energy C1s peak corresponds to the reference value of 284.8 eV.

Fig. 5a, b, e, and g denote the elements present in zeolite 13X [35,36]. The Na 2 s-Al 2p spectra (Fig. 5a) reveal two doublet signals corresponding to (i) Na oxides and Na 2 s orbitals and (ii) $Al(OH)_3$ and Al_2O_3 compounds, with binding energies of 61.8, 63.8, 74.3 and 76.2 eV, respectively [37]. The Al 2p and Si 2p occupied state spectrum (Fig. 5b) display two peaks with binding energies at 102.2 eV and 119.1 eV that can be assigned to the SiO-O-Al bond and Si 2p orbital, respectively [35,36,38]. Fig. 5e displays the NaKLL signal at 497.7 eV, indicating the presence of Na in the thin zeolite crystal, whereas the Na 1 s orbitals are shown in Fig. 5g at 1071.5 eV [38].

The catalyst composed of Ru and Ti elements is represented in Fig. 5c, d, and e [18]. The C1s - Ru 3d combined spectrum (Fig. 5c) includes the C1s reference signal at 284.8 eV and the differences in Ru 3d binding energies at: (i) 280.2 and 281.6 eV, related to the Ru $3d_{5/2}$ orbital, and (ii) 289.3, and 292.8 eV, related to the Ru $3d_{3/2}$ orbital. The Ru 3d spectrum reveals the existence of both zero-valent Ru metal and various Ru oxide states [18,39]. Confirmation of this element is also evident from the integrated spectrum of Ti 2p - Ru 3p shown in Fig. 5d. The peaks at 458.4 and 464.2 eV have been assigned to Ti $2p_{3/2}$ and Ru $3p_{3/2}$ + Ti $2p_{1/2}$ orbitals, respectively, due to the screening effect at the charge-transfer configurations of Ru and Ti atoms. Furthermore, there is a satellite zone between 468 and 481 eV, belonging to the main Ti 2p and Ru 3p occupied states, and a peak at 485.4 eV, corresponding to a Ru $3p_{1/2}$ orbital [40]. The deconvolution of the O 1 s spectrum (Fig. 5f) discerns two peaks, O1 at 529.7 eV and O2 at 531.4 eV, which are related to the zeolite 13X oxide species, Ru-oxides, and defects in the semiconductor [35,40].

3.2. Photocatalytic activity

The pseudo-first-order kinetic model was able to describe the kinetics of CO_2 reduction for all catalytic reactions (0.921 < coefficient of determination (R^2) < 0.993). The kinetic parameters and efficiency indicators are presented in Table S5. The main product of CO_2 hydrogenation was CH_4, with only a residual presence of C_2H_6 (less than 0.9%). Furthermore, CO or other higher hydrocarbon levels remained below the analytical detection limit.

3.2.1. Effect of the photocatalytic material composition

Fig. 6 depicts the thermo-photocatalytic activity of several catalysts (30 mg, 150 °C, and 0.75 W of sunlight radiant power) containing different RuO_2 loads over TiO_2 and $SrTiO_3$ semiconductors (with [Ru]: [semiconductor] mass ratios of 1:10, 2:10, and 3:10) towards CO_2 hydrogenation into CH_4 (Table S5, experiments #1.1 to #1.6). Despite using identical Ru-to-semiconductor mass ratios, the ICP-IOS analysis revealed different amounts of Ru within the semiconductors. Specifically, while the $RuO_{2(x\%)}$:TiO_2 materials displayed estimated RuO_2 contents of 6.8, 13.4, and 18.3 wt%, the $RuO_{2(x\%)}$:$SrTiO_3$ materials exhibited estimated RuO_2 contents of 10.1, 18.6, and 21.4 wt% (Table S2). These results point out differences of 33%, 28%, and 14% when comparing the $RuO_{2(x\%)}$:TiO_2 against $RuO_{2(x\%)}$:$SrTiO_3$ using [Ru]: [semiconductor] mass ratios of 1:10, 2:10, and 3:10, respectively. According to the manufacturer's specifications, the $SrTiO_3$ nanocuboids

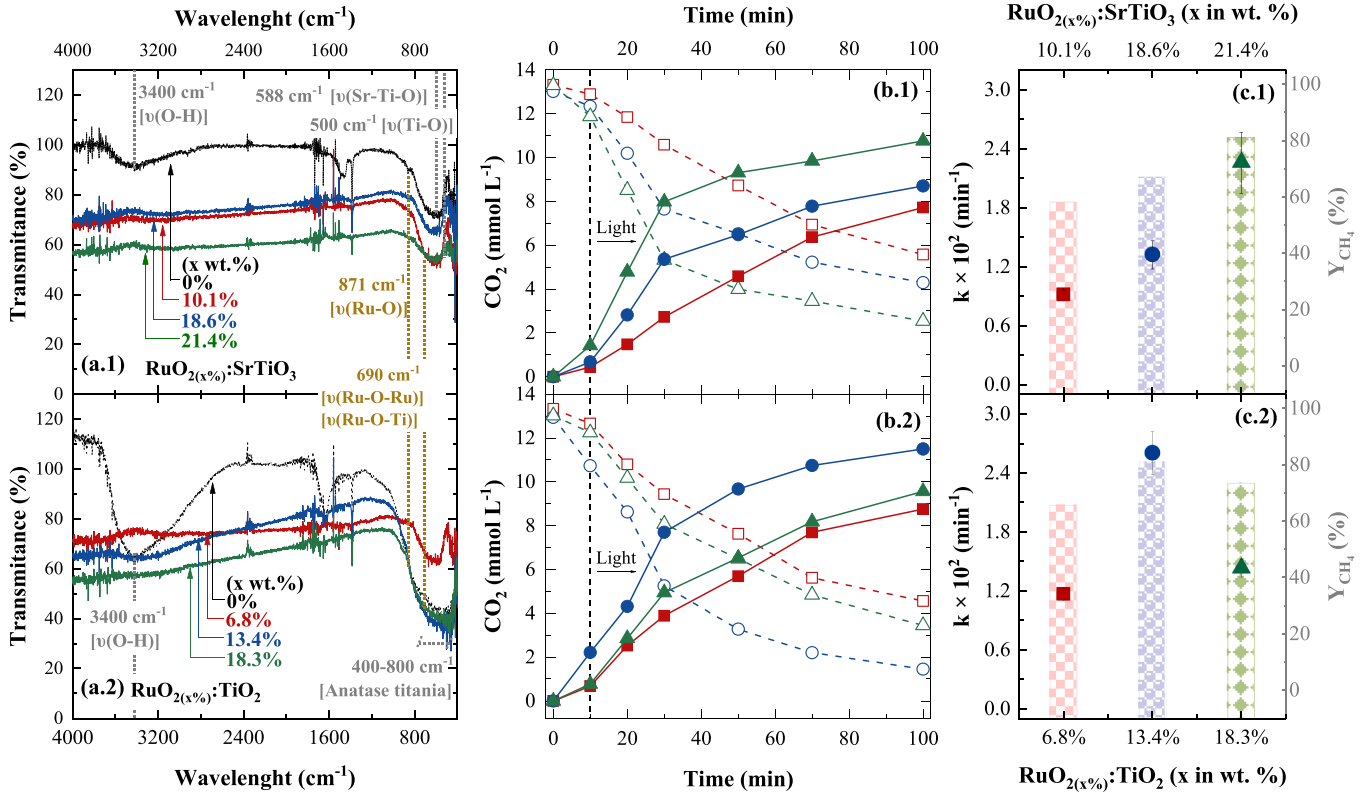

Fig. 6. Influence of the Ru load on the performance of (.1) $RuO_{2(x\%)}$:$SrTiO_3$ (x = 10.1%-■, 18.6%-●, and 21.4%-▲) and (.2) $RuO_{2(x\%)}$:TiO_2 (x = 6.8%-■, 13.4%-●, and 18.3%-▲) photocatalysts, considering: (a) FTIR spectra; (b) temporal conversion of CO_2 (open symbols) into CH_4 (closed symbols) by solar-driven thermo-photocatalysis; and (c) pseudo-first-order kinetic constants for CO_2 reduction (symbols) and CH_4 production yields (bars). Operating conditions for methanation reaction: V = 40 mL; P_{CO2} = 0.32 bar; P_{H2} = 1.28; 30 mg of photocatalyst; T = 150 °C; and RP = 0.75 ± 0.01 W.

(99% purity) feature a size of less than 100 nm, a surface area of 11.4 m^2 g^{-1}, and a density of 4.8 g cm^{-3}. In contrast, the TiO_2 nanospheres (95% purity) present a size of about 12 nm, a surface area of 300 m^2 g^{-1}, and a density of 4.2 g cm^{-3}. According to Asundi et al. [41], impurities in commercial heterogeneous catalyst supports can influence the catalyst properties. Noteworthy observations by Erwin et al. [42] indicate that the light absorption process and loading efficiency are influenced by three primary factors: surface morphology, nanocrystal shape, and surfactants in the growth solution.

The FTIR spectra for different photocatalyst compositions are shown in Fig. 6a. The unsupported $SrTiO_3$ spectrum exhibited the characteristic vibration absorption of υ(Sr-Ti-O) at 588 cm^{-1} and υ(Ti-O) at 500 cm^{-1} [43]. Commercial TiO_2 displays characteristic broadband of around 400–800 cm^{-1}, indicative of anatase titania [33,44]. FTIR analysis detected shifts or changes in the absorption peaks upon metal addition, suggesting chemical modifications of the material. These alterations may arise from interactions between Ru metal and titanium semiconductors, leading to vibrational and bonding characteristics changes. The bands at around 690 cm^{-1} and 871 cm^{-1} are strengthened due to the υ(Ru-O-Ru)/υ(Ru-O-Ti) and υ(Ru-O) vibrations [33,45], whose intensity increases proportionally with the amount of Ru doped in the semiconductors. Furthermore, an elongation of the band between 3000 cm^{-1} and 3757 cm^{-1} represents the stretching vibrations of -OH groups, confirming the synthesis of hydrated metal oxides and corroborating the occurrence of RuO_2 loading [46,47].

TiO_2 and $SrTiO_3$ semiconductors can generate reactive species under illumination, enabling their participation in CO_2 conversion reactions. Besides, the CO_2 conversion efficiency depends on factors like catalyst morphology, surface area, loading, and co-catalysts. Optimisation of these factors is crucial for enhancing the photocatalytic performance of TiO_2 and $SrTiO_3$ towards thermo-photocatalytic CO_2 reduction. Thus, the RuO_2 loading was varied to compare the activities of these semiconductors (Fig. 6b-c). The observed CO_2 conversions ranged from 58.1% to 80.9% for RuO_2:$SrTiO_3$ (Table S5, experiments #1.1 to #1.3) and from 65.8% to 80.8% for RuO_2:TiO_2 (Table S5, experiments #1.4 to #1.6), after 100 min at 150 °C. The corresponding pseudo-first-order kinetic constants for CO_2 reduction vary from $(0.92 \pm 0.05) \times 10^{-2}$/$(1.17 \pm 0.06) \times 10^{-2}$ to $(2.3 \pm 0.3) \times 10^{-2}$/$(2.6 \pm 0.2) \times 10^{-2}$ min^{-1} for RuO_2:$SrTiO_3$/RuO_2:TiO_2. When the [Ru]:[$SrTiO_3$/TiO_2] mass ratio increases from 1:10–2:10, a considerable increase of 29%/55% in the kinetic constant and 9%/15% in the thermo-photocatalytic CO_2 conversion can be observed for the RuO_2:$SrTiO_3$/RuO_2:TiO_2 catalysts (Table S5, experiments #1.1–1.2/#1.4–1.5). The enhanced proprieties and performance of TiO_2 and $SrTiO_3$ as photocatalysts, when loaded with increased amounts of RuO_2, can be attributed to improved charge separation, extended light absorption range, and raised surface reactivity [12]. However, a further increment in the mass ratio from 2:10–3:10 had different effects on the semiconductors. In the case of the RuO_2:$SrTiO_3$ catalyst, the 100-min CO_2 conversion continued to increase by approximately 14%, accompanied by a substantial 77% enhancement in the kinetic constant. Conversely, on the RuO_2:TiO_2 catalyst, the CO_2 conversion decreased, suggesting an overload of Ru particles in the semiconductor, impairing the photocatalytic performance, including increased charge carrier recombination, altered band structure, and reduced material stability [48]. Therefore, when comparing the two catalysts, it was found that the $SrTiO_3$-based catalyst demanded a higher amount of Ru to attain the same level of CO_2 conversion as the TiO_2-based catalyst, being required 50% more in terms of initial Ru mass ratio and 60% more in terms of final impregnated Ru concentration.

To effectively compare the two semiconductors in structured photocatalysts, performing their analysis under optimised metal oxide loading conditions is essential. Over-loading can lead to a decrease in catalyst performance due to increased electron-hole recombination and can negatively affect the energy levels, compromising the material's structural integrity [48]. In this sense, the thermo-photocatalysts featuring the best performance, concerning Ru concentration in the titanium-based semiconductors, are $RuO_{2(13.4\%)}$:TiO_2 and $RuO_{2(21.4\%)}$:$SrTiO_3$ with 100-min CO_2 conversions of 80.8% and 80.9% and kinetic constants for CO_2 reduction of $(2.6 \pm 0.2) \times 10^{-2}$ and $(2.3 \pm 0.3) \times 10^{-2}$ min^{-1} (Table S5, experiments #1.3 and #1.5), respectively. Because Ru belongs to the category of noble metals and the TiO_2 semiconductor requires a smaller amount to sustain optimal catalytic activity, the $RuO_{2(13.4\%)}$:TiO_2 material was used to prepare the hybrid photocatalyst/adsorbent material. Integrating noble metals with semiconductors yields high-performing composites for converting CO_2 into low-carbon fuels [49]. It should be noted that, due to the predominance of the Sabatier reaction, only the CH_4 production profile is presented in the remaining experiments.

3.2.2. *Effect of the bifunctional photocatalyst/adsorbent material composition*

Fig. 7 shows the thermo-photocatalytic activity of the bifunctional material (30 mg, 150 °C, 0.75 W of sunlight radiant power), with different contents the $RuO_{2(13.4\%)}$:TiO_2 catalyst on the zeolite 13X adsorbent ([RuO_2:TiO_2]:[Z13X] mass ratios of 1:10, 2:10, 3:10, 4:10, 5:10, and 10:0, equivalent to ca. 9%, 17%, 23%, 30%, 34% and 100% of active catalyst), prepared by wet impregnation – WIM (Fig. 7a, Table S5 experiments #2.1 to #2.4) and solid-state impregnation – SIM (Fig. 7b, Table S5 experiments #2.5 to #2.8) methods. As the zeolite 13X does not participate in the methanation reaction, the specific CH_4 production results are expressed in mmol of CH_4 per gram of active catalyst, *i.e.*, RuO_2:TiO_2 (mmol CH_4 $g^{-1}_{active\_cat}$).

When the impregnation procedures are compared, WIM results in a lower catalytic activity for the same bifunctional material composition. The inhibition of the methanation reaction was most likely due to inadequate water removal during the drying step. The presence of water in the zeolite can negatively affect the sintering of Ru during calcination, thereby compromising the formation of Ru-oxide [50]. The strong interaction between water and the zeolite 13X structure [64] poses challenges for removing or desorbing water molecules from the WIM-prepared hybrid material during the drying and calcination processes. In addition, the potential remaining water in the zeolite may compete with CO_2 for adsorption sites during the reaction. When using WIM, pseudo-first-order kinetic constants below 0.8×10^{-2} min^{-1} (Fig. 7a.2) and CO_2 conversions below 52% (Fig. 7a.3) were achieved, regardless of the photocatalyst content in the hybrid material. In the absence of zeolite 13X, the overall performance was lower than that of the photocatalytic material alone (Table S5 experiment #1.5) despite the bifunctional material producing more CH_4 per mass of the active photocatalyst.

In contrast, using SIM to synthesise the hybrid material positively impacted the CO_2 conversion efficiency, as depicted in Fig. 7b, which can be attributed to the combined effect of adsorption and thermo-photocatalysis, resulting in a higher catalytic activity (Table S5, experiments #2.5 to #2.9). When the [RuO_2:TiO_2]:[Z13X] mass ratio increased from 2:10–4:10, the CO_2 conversion surged from 23.6% to 88.0%, corresponding to a rise of one order of magnitude in the initial CO_2 reduction rate (0.035 ± 0.002–0.36 ± 0.07 mM min^{-1}). However, increasing the mass ratio to 5:10 decreased the CO_2 conversion by 64%, indicating that excessive amounts of the catalyst inhibited the photocatalytic methanation reaction. Catalyst overloading in zeolite 13X intensifies particle agglomeration, electron-hole pair recombination, reduced particle illumination [51], and pore blockage in zeolite 13X [30]. In this situation, the excess catalyst in the hybrid material can further hinder CO_2 adsorption. Therefore, raising the photocatalyst-to-adsorbent ratio enhanced CO_2 methanation until further increments impaired the hybrid process. Accordingly, the best proportion of photocatalyst-to-adsorbent using SIM as the synthesis process was 29-to-71 wt%. When comparing the reaction using the $RuO_{2(13.4\%)}$:TiO_2 photocatalyst with that using the bifunctional $RuO_{2(4.0\%)}$:$TiO_{2(26.3\%)}$/Z13X material (Table S5, experiments #1.5 and #2.7), it

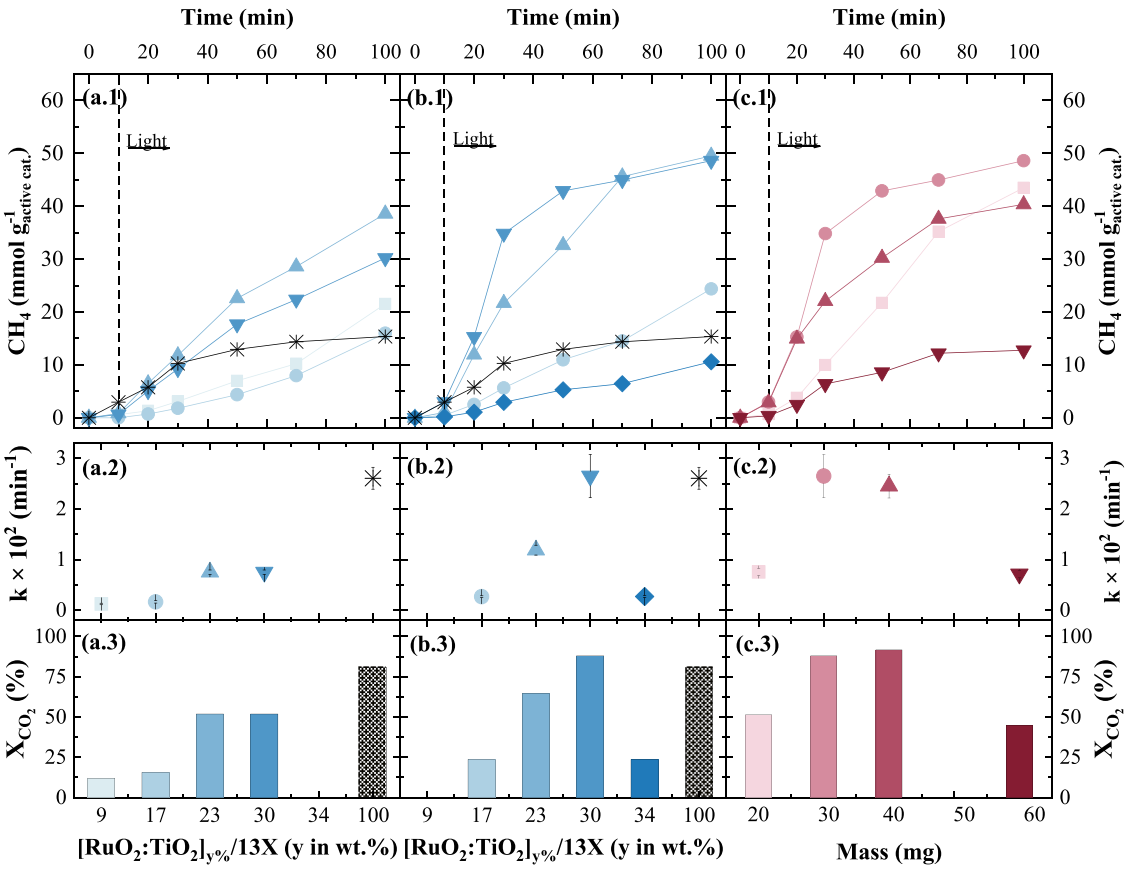

Fig. 7. Representation of: (.1) specific CH_4 production over time via solar-driven thermo-photocatalysis; (.2) pseudo-first-order kinetic constant for CO_2 reduction; and (.3) overall CO_2 conversion at 100-min, using different percentages of the active photocatalyst (9-□, 17-○, 23-△, 30-▽, 34-◇, and 100-✳ wt% of RuO_2:TiO_2) in the RuO_2:TiO_2/Z13X bifunctional composite (30 mg), prepared by (a) wet-state impregnation method (WIM) and (b) solid-state impregnation method (SIM). (c) Variation of the $RuO_{2(4.0\%)}$:$TiO_{2(26.3\%)}$/Z13X material mass (20-□, 30-○, 40-△, and 60-▽ mg), prepared by SIM. Operating conditions: $V = 40$ mL; $P_{CO2} = 0.32$ bar; $P_{H2} = 1.28$; $T = 150$ °C; and $RP = 0.75 \pm 0.01$ W.

was verified that CO_2 conversion was maintained while using only 29 wt % of the catalyst, resulting in a specific CH_4 production of about 48.6 mmol CH_4 $g^{-1}_{active\_cat}$, 29.2 mmol CH_4 $g^{-1}_{active\_cat}$ h^{-1}, and 309 mmol CH_4 g^{-1}_{Ru} h^{-1}. This represents a significant decrease of up to 3.4-fold in the amount of Ru required while still keeping a pseudo-first-order kinetic constant of ca. $(2.6 \pm 0.4) \times 10^{-2}$ min^{-1} (Fig. 7b.2) and a CO_2 reduction efficiency of ca. 88% (Fig. 7b.3).

For comparison, a bifunctional material with a 30 wt% of the $RuO_{2(21.4\%)}$:$SrTiO_3$ photocatalyst (the best composition using this semiconductor) and 70% the zeolite 13X adsorbent was also prepared by SIM (Table S5, experiment #2.9). The hybrid $RuO_{2(6.5\%)}$:$SrTiO_{3(23.8\%)}$/Z13X material achieves a CO_2 conversion of 84.7% after 100 min at 150°C, with a kinetic constant of $(2.3 \pm 0.2) \times 10^{-2}$ min^{-1} and an initial reaction rate of 0.30 ± 0.04 mM min^{-1}, resulting in specific CH_4 production yields of 48.9 mmol CH_4 $g^{-1}_{active\_cat}$, 29.3 mmol CH_4 $g^{-1}_{active\ cat}$ h^{-1}, and 180 mmol CH_4 g^{-1}_{Ru} h^{-1}. Both $SrTiO_3$ and TiO_2 semiconductors lead to similar CO_2 thermo-photocatalytic reduction efficiencies by impregnating zeolite with a catalyst. However, it is noteworthy that the $RuO_{2(6.5\%)}$:$SrTiO_{3(23.8\%)}$/Z13X material demands a larger Ru quantity, resulting in a 1.7-fold reduction in CH_4 generation relative to the Ru mass when compared to the $RuO_{2(4.0\%)}$:$TiO_{2(26.3\%)}$/Z13X material. Hence, this bifunctional material was used in subsequent experiments.

Fig. 7c illustrates the influence of the $RuO_{2(4.0\%)}$:$TiO_{2(26.3\%)}$/Z13X mass (20, 30, 40, and 60 mg) on the thermo-photocatalytic CO_2 methanation (150 °C, and 0.75 W of sunlight radiant power) (Table S5, experiments #2.7 and #3.1 to #3.3). The CO_2 conversion and the kinetic constant rise significantly from 51.4% to 88.0% and from $(0.75 \pm 0.07) \times 10^{-2}$ to $(2.6 \pm 0.4) \times 10^{-2}$ min^{-1}, respectively, when the material mass was increased from 20 to 30 mg (Fig. 7c.3 and Fig. 7c.2, respectively). However, when the material mass was further raised to 40 mg, the influence on the methanation efficiency became minimal ($X_{CO2} = 91.7\%$; $k = (2.5 \pm 0.2) \times 10^{-2}$ min^{-1}). As zeolite is a non-transparent solid, an excess of this material within the photoreactor can reduce its photocatalytic effectiveness [52]. Accordingly, 60 mg of the hybrid material had a detrimental effect on the methanation reaction due to the presence of shadow zones between the particles, leading to a lower specific CH_4 production (Fig. 7c.1). Hence, 30 mg of the bifunctional material was selected as the bifunctional material mass for the subsequential tests.

The adsorption and thermo-photocatalytic effects of the hybrid $RuO_{2(4.0\%)}$:$TiO_{2(26.3\%)}$/Z13X (30 mg) enhances the CO_2 methanation (88.0%, after 100 min at 150°C), even with a small amount of active photocatalyst (9.7 mg), and specific CH_4 yields of 29.2 mmol CH_4 $g^{-1}_{active\_cat}$ h^{-1}, 712 mmol CH_4 $g^{-1}_{active\_cat}$ h^{-1} $L^{-1}_{reactor}$, and 309 mmol CH_4 g^{-1}_{Ru} h^{-1}. Similar high CO_2 conversions of around 90% have been reported in other studies after 120 min of photo-thermal catalysis in batch mode, using $Ru_{(5\%)}$/black TiO_2 photocatalyst (20 mg; 0.4 mPa; $[N_2]$:$[H_2]$:$[CO_2]$ = 4:5:1) at 200 °C (estimated CH_4 production of 239 mmol

$CH_4\ h^{-1}\ g_{cat}^{-1}\ L_{reactor}^{-1}$) [13] and $RuO_{2(0.4\%)}/SrTiO_3$ photocatalyst at 150 °C (14.6 mmol $CH_4\ h^{-1}\ g_{cat}^{-1}$) [14]. Nonetheless, the specific CH_4 production rate obtained in this work is about 3.0 [13] and 2.0 [14] times higher when only the mass of the active catalyst is considered. Regarding thermal catalysis, CO_2 conversions of 80% and 65% in continuous mode were attained using the $Ru_{(2.5\%)}/TiO_2$ catalyst at 325 °C (21.2 mmol $CH_4\ h^{-1}\ g_{cat}^{-1}$) [53] and $Ru_{(5\%)}$/r-TiO_2 catalyst at 300 °C (estimated production of 185 mol $CH_4\ h^{-1}\ g_{cat}^{-1}$) [54], respectively. Ge et al. [55] reported that Ru/$HxMoO_3$-y (with a 4 wt% Ru loading) photocatalyst produced 20.8 mmol $CH_4\ g_{cat}^{-1}\ h^{-1}$ or 520 mmol $CH_4\ g_{Ru}^{-1}\ h^{-1}$ (CO_2 conversion of about 17%) under Vis-NIR light irradiation at 140 °C in continuous mode. When comparing the current study's findings with this specific outcome [55], it was verified that the CO_2 conversion is about 80% higher, and the CH_4 production rate is about 1.4 times higher if considering the mass of the active catalyst.

3.2.3. *Effect of illumination source*

Solar-driven photocatalysis offers an undeniably attractive approach for leveraging renewable energy sources to enhance catalytic processes that target synthesising value-added chemicals. Nevertheless, complementary light sources should also be explored because, despite being sustainable and inexhaustible, solar light intensity is inconsistent depending on daytime, season, and geographic location. Miniaturised monochromatic light sources have emerged as a promising alternative to foster catalytic reactions, providing a tailored irradiance profile that optimises catalytic surface illumination and overall efficiency [56,57]. However, the effects of different light sources on CO_2 conversion remain poorly understood. In this regard, Fig. 8 provides insights into the performance of CO_2 methanation (30 mg of $RuO_{2(4.0\%)}$:$TiO_{2(26.3\%)}$/Z13X; 150 °C) under different lighting devices featuring distinct radiant powers (*RP*): (i) polychromatic simulated sunlight between 280 and 800 nm (Table S5, experiments #2.7 and #4.1 to #4.3 for RP from 0.42 to 1.090 W); (ii) monochromatic visible LED at 405 nm (Table S5, experiments #4.4–4.6 for RP from 0.055 to 0.55 W); and (iii) monochromatic UV LED at 365 nm (Table S5, experiments #4.7 to #4.9 for RP from 0.053 to 0.55 W).

Considering the mutual *RP* value of 0.5 W (within the overlapping interval of 0.42–0.55 W), the different illumination sources can be ranked in terms of initial CO_2 reduction rate (estimated from the linear regression of r_0 vs. RP) from most to least efficient, as follows: 365 nm

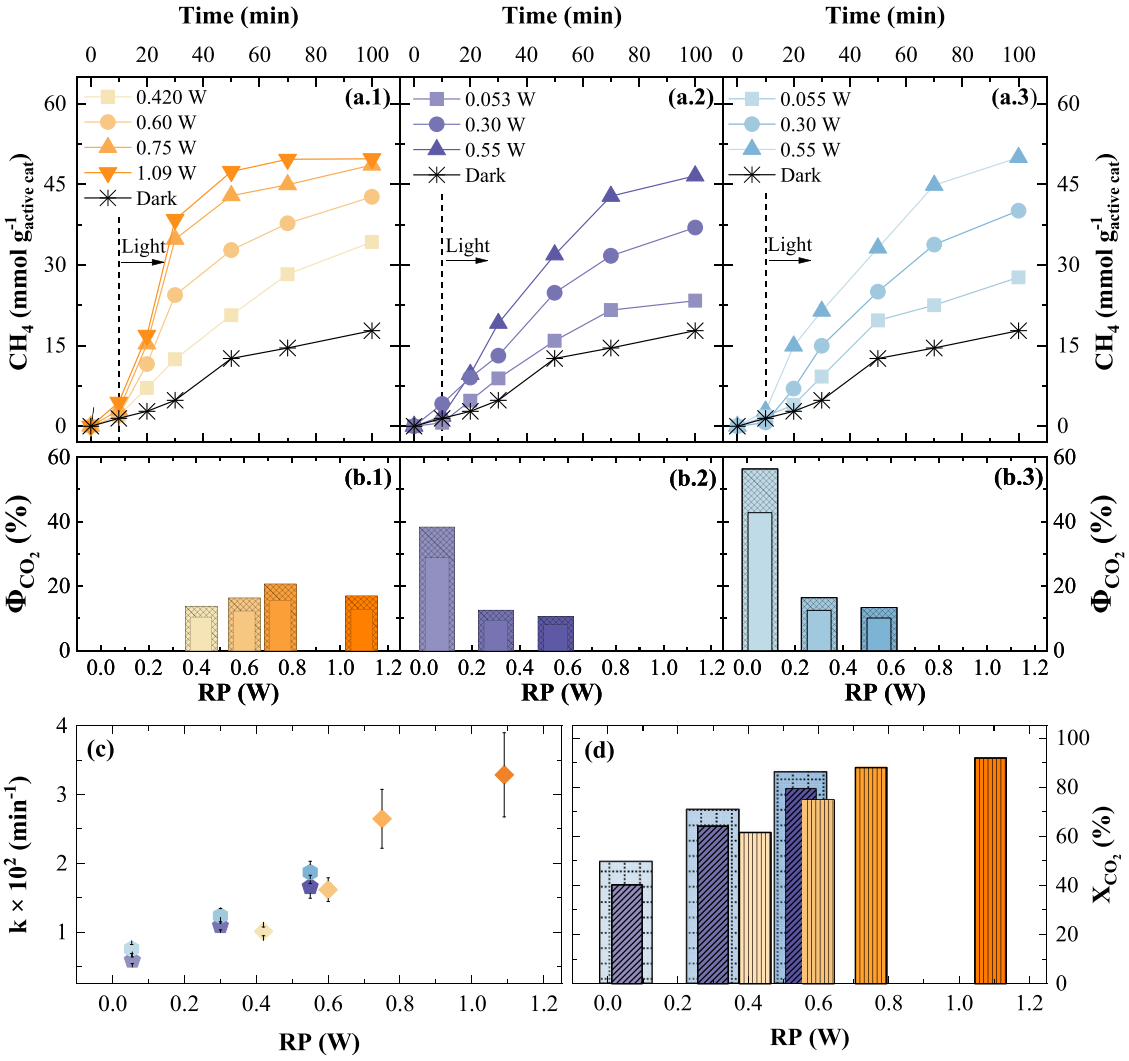

Fig. 8. Representation of (a) specific CH_4 production over time via thermo-photocatalysis and (b) apparent photonic efficiency ($\Phi_{CO_2}^{APE}$, solid bars) and apparent quantum yield ($\Phi_{CO_2}^{AQY}$, patterned bars), (c) pseudo-first-order kinetic constant for CO_2 reduction, and (d) overall CO_2 conversion at 100-min, as a function of the radiant power (RP), for different illumination sources: (.1) polychromatic (280–800 nm) sunlight simulator (◆, ▥); and monochromatic (.2) 405 nm LED (⬟, ▨), and (.3) 365 nm LED (⬢, ▦). Operating conditions: $V = 40$ mL; $P_{CO2} = 0.32$ bar; $P_{H2} = 1.28$; 30 mg of $RuO_{2(4.0\%)}$:$TiO_{2(26.3\%)}$/Z13X composite; and $T =$ 150 °C.

LED (0.24 mM min^{-1}) > 405 nm LED (0.21 mM min^{-1}) > sunlight (0.18 mM min^{-1}). This slight difference between the lighting devices agrees well with the DRS analysis (Fig. 4), where it was disclosed that the bifunctional material has a high absorption capacity across all the UVA-visible spectrum, with a particularly favourable absorption in the UVA region due to the TiO_2 semiconductor [51]. Regardless of the irradiation source, Fig. 8a and c-d demonstrates that: (i) a superior performance of the CO_2 methanation reaction at 150ºC is reached via thermo-photocatalysis, considering $RP \geq 0.30$ W, compared to thermal catalysis under dark conditions; and (ii) the photocatalytic activity increases proportionally to the *RP* reaching within the reactor, denoting the importance of the photochemical pathway when combining thermal catalysis with photocatalysis. Overall, the pseudo-first-order kinetic constant for CO_2 reduction increases as a function of *RP* as follows (Fig. 8c): (i) from $(1.0 \pm 0.1) \times 10^{-2}$ to $(3.3 \pm 0.6) \times 10^{-2}$ min^{-1}, considering the *RP* range from 0.42 to 1.09 W, for polychromatic irradiation; and (ii) from $(0.59 \pm 0.05) \times 10^{-2}/(0.76 \pm 0.07) \times 10^{-2}$ to $(1.7 \pm 0.2) \times 10^{-2}/(1.9 \pm 0.02) \times 10^{-2}$ min^{-1}, considering the *RP* from 0.05 to 0.55 W, for monochromatic irradiation at 405/365 nm.

In the case of polychromatic radiation (Fig. 8c), the higher the incoming sunlight power, the greater the $RuO_{2(4.0\%)}$:$TiO_{2(26.3\%)}$/Z13X photo-responsiveness, with the initial CO_2 reduction rate being proportional to the *RP* by a factor of: (i) 0.67 mM min^{-1} W^{-1} ($R^2 = 0.959$), from an *RP* of 0.42–0.75 W (Table S5, experiments #4.1, #4.2, and #2.7); and (ii) 0.25 mM min^{-1} W^{-1}, from an *RP* of 0.75–1.09 W (Table S5, experiments #2.7 and #4.3). Furthermore, raising the *RP* from 0.42 to 0.75 W gradually enhanced the CO_2 conversion after 100 min, from 61% to 88.0%, with a 162% increase in the kinetic constant. A further increment up to 1.09 W upholds a similar methanation yield of 92%, with a slight 24% increase in the kinetic constant (Fig. 8a.1, c, and d). So, when using high sunlight power, there is a point at which the CO_2 conversion efficiency reaches a maximum plateau, and the reaction rate becomes virtually irradiance-independent (Fig. 8d). This phenomenon can be attributed to the internal conversion transitions to lower excited states before any radiative emission process [58]. In this case, vibrational relaxation in the upper excited state occurs before charge transfer, and as a result, the excess absorbed photons cannot be effectively utilised [59]. In the case of monochromatic irradiation (Fig. 8a.2, a.3, c and d), CH_4 production consistently increased in direct proportion to the *RP* values within the range of 0.05–0.55 W, which represents the minimum and maximum power allowed by the LED power supply. These *RP* values were relatively low; therefore, the observed trend aligns with the results obtained for simulated sunlight at low irradiance levels. Within this range, the initial CO_2 reduction rate is proportional to the *RP* values: (i) 0.29 mM min^{-1} W^{-1} for 405 nm LED; and (ii) 0.31 mM min^{-1} W^{-1} for 365 nm LED. According to Sarina et al. [60], only photons with sufficient energy higher than the lowest unoccupied molecular orbitals' energy level can initiate reactions. Both polychromatic (280–800 nm) and monochromatic (365 and 405 nm) radiation provided sufficient energy to activate the photocatalyst, as evidenced by the increasing reactivity with increasing irradiance. Photocatalysis allows reactions to occur at reduced temperatures by leveraging the electron photoexcitation effect, which concurrently enhances the adsorption of the hybrid material. Therefore, in the specific domain of direct thermo-photocatalysis, wherein Ru-oxide nanoparticles are integrated into TiO_2 supported by zeolite 13X, the substantial contribution of photon-electron excitation plays a paramount role in accomplishing a noteworthy CO_2-to-CH_4 conversion efficiency at 150 ºC.

The light utilisation efficiency of the thermo-photocatalytic system was assessed by estimating the following parameters: (i) apparent photonic efficiency ($\Phi_{CO_2}^{APE}$), which is the ratio between the moles of CO_2 converted and the moles of photons reaching the photoreactor; and (ii) apparent quantum yield ($\Phi_{CO_2}^{AQY}$), which is the ratio between the moles of CO_2 converted and the moles of photons absorbed by the photocatalyst (detailed calculation can be found in the Supplementary Material). These values are represented in Fig. 8d. When comparing the $\Phi_{CO_2}^{APE}$ with $\Phi_{CO_2}^{AQY}$, it is evident that *ca.* 75% of the incoming radiation to the photoreactor is effectively utilised by the bifunctional photocatalyst/adsorbent material, regardless of the illumination source tested. Both parameters differ only in the apparent fraction of light absorbed by the photocatalyst, which is remarkably similar for all lighting devices (0.75–0.76), in agreement with the UV-Vis DRS analysis of the hybrid material (Fig. 4). Consequently, their behaviour is nearly identical, and the ensuing discussion will mainly focus on $\Phi_{CO_2}^{AQY}$.

With respect to polychromatic radiation, the $\Phi_{CO_2}^{AQY}$ values gradually increase from 13.8% to 20.7% within the *RP* range of 0.42–0.75 W. However, as the *RP* is further extended to 1.09 W, there is an excess of incident energy, leading to a reduction in the overall quantum efficiency, with $\Phi_{CO_2}^{AQY}$ dropping to 17.0% (Fig. 8b.1). On the other, for monochromatic radiation at 405/365 nm, as the *RP* value increases from 0.05 < 0.30 < 0.55 W, the $\Phi_{CO_2}^{AQY}$ values decrease from 38.4%/56.4% > 12.6%/16.5% > 10.7%/13.4% (Fig. 8b.2 and b.3). Nevertheless, it should be noted that at the lowest *RP* of 0.05 W, the methanation reaction proceeds preferentially via thermal catalysis, as can be inferred from the similar CH_4 production profiles observed under both lighting and dark conditions (Fig. 8a.2 and a.3). Therefore, in the presence of low photon flux, the $\Phi_{CO_2}^{AQY}$ values are over-estimated. In this sense, if these over-hyped values are disregarded, as they are clearly affected by external heating rather than incoming irradiation, it could be verified that the simulated sunlight presents the highest $\Phi_{CO_2}^{APE}$ and $\Phi_{CO_2}^{AQY}$ values, reaching 15.6% and 20.7% for an *RP* of 0.75 W, respectively. The high absorption coefficients and energy transfer capabilities of Ru dinuclear complexes in the visible region contribute to the increased photoreaction efficiency through multi-electron reduction processes and efficient charge separation, as described by Wouters et al. [61]. The results found in the current work are consistent with the $\Phi_{CO_2}^{AQY}$ values reported in the literature regarding photocatalytic methanation, such as 25.8% for f-C_3N_4/OV-Ti_3AlC_2 [62] and 12.4% for 0.35-BT-30 [63] materials. The comparable performance of the different radiation sources confirms the excellent photoresponse of the hybrid material, which can absorb radiation in the UVA-vis region, according to DRS analysis. The electronic modification of the catalyst by introducing metal oxide nanoparticles influences the tuning of the photoresponse wavelength by affecting the dynamics of electron-hole separation at the interface [58].

The proposed hybrid material exhibited equally high photoactivity towards CO_2 methanation when exposed to energy-efficient LEDs at 405 and 365 nm or direct sunlight. This versatility provides some advantages for real-scope applications, as the operating system can utilize natural solar radiation during the day and switch to miniature light sources at night.

Solar-driven thermo-photocatalysis harnesses renewable energy and offers the most favourable combination of CO_2 conversion (88.0%) and apparent photonic efficiency (15.6%) compared to other lighting sources. Consequently, simulated sunlight at 0.75 W was utilised for the following experiments.

3.2.4. *Effect of temperature*

Raising the temperature can boost CO_2 photoreduction by: (i) avoiding electron-hole recombination, which allows efficient charge separation and utilisation of photogenerated carriers; (ii) enhancing diffusion rates, which facilitate the transport of reactants/products to and from the photocatalyst's active sites; (iii) promoting product desorption, which frees up active sites for further catalytic reactions; and (iv) augmenting the likelihood of reactant molecule collisions on the photocatalyst surface, which leads to higher reaction rates [64,65]. However, higher temperatures can also reduce the adsorption capacity due to weaker interactions between the adsorbate and the adsorbent

[66]. Thus, temperature has two opposing effects on the hybrid material: (i) a positive effect on the reaction rate due to increased particle excitation; and (ii) a negative effect on the adsorption ability. Accordingly, this section investigates the impact of different temperatures on the performance of CO_2 hydrogenation into CH_4 over bifunctional $RuO_{2\,(4.0\%)}$:$TiO_{2(26.3\%)}$/Z13X material (30 mg) via adsorption/thermal catalysis (under dark conditions) and adsorption/thermo-photocatalysis (0.75 W of sunlight radiant power). The main findings are presented in Fig. 9 and Table S5 (experiments #2.7 and #5.1–5.9).

As expected, the methane yield increased with temperature, indicating that higher reaction temperatures favour the CO_2 hydrogenation reaction (Fig. 9a). The thermal conversion of CO_2 into methane is only observed at temperatures $\geq$ 150 °C, achieving a low value of 33% after 100 min at such temperature due to slow kinetics. As the temperature has risen from 150 to 250 °C under dark conditions, the pseudo-first-order kinetic constant increased from (0.44 ± 0.06) × 10^{-2} to (3.3 ± 0.4) × 10^{-2} (Table S5, experiments #5.3–5.5). In the case of thermo-photocatalysis, the fact that CH_4 generation can be detected from 50 °C onwards, with specific CH_4 production rates of 0.1/14.6 mmol $g^{-1}_{active\_cat}$ h^{-1} at 50/100 °C, highlighting the positive effect of solar-driven photocatalysis at lower temperatures (Table S5, experiments #5.6 and #5.7). As the temperature rose from 150 to 250 °C under sunlight, the kinetic constant increased from (2.6 ± 0.4) × 10^{-2} to (3.9 ± 0.3) × 10^{-2} min^{-1} (Table S5, experiments #2.7 and #5.8). It should be emphasised that at 150 °C, the CO_2 reduction reaction was 2.7-fold more efficient and 6.0-fold faster via thermo-photocatalysis than thermal catalysis (Table S5, experiments #2.7 and #5.3). Integrating heterogeneous thermo-photocatalysis into a hybrid approach has gained considerable attention due to its ability to convert CO_2 in the gas phase under relatively moderate operating conditions [67,68]. In addition, zeolites exhibit a higher capacity for CO_2 adsorption at lower temperatures. These zeolites demonstrate remarkable adsorption abilities at medium temperatures around 150 °C [66]. This study highlights an excellent approach to fostering the methanation reaction by combining CO_2 capture and thermal photoconversion over new bifunctional material, showcasing the potential of this hybrid strategy.

The apparent activation energy (E_a) (calculation formulas are available in the Supplementary Material) of thermal catalysis was estimated at 23 ± 9 kJ mol^{-1} for temperatures ranging from 150 to 250 °C (Fig. 9b). In comparison, the thermo-photocatalysis exhibits two distinct phases with E_a values of 41 ± 4 kJ mol^{-1} and 9 ± 3 kJ mol^{-1}, for temperatures between 50 and 150 °C and 150–250 °C, respectively (Fig. 9b). This discrepancy can be attributed to the effect of temperature on the hybrid material. Enhanced adsorption at low temperatures can improve the reaction conditions but compromise the catalytic performance. Karelovic and Ruiz [69] reported an E_a of 71.1 kJ mol^{-1} (17.0 kcal mol^{-1}) for $Rh_{(3\ wt\%)}/TiO_2$ catalyst in thermal catalysis at the range of 100–165 °C. According to Ullah et al. [70], E_a decreased by 20%, from 74.8 to 60.2 kJ mol^{-1}, when comparing dark and light conditions using the Co_{10}/La_{15}-TiO_2 catalyst in the temperature range of 200–350 °C. In the current study, the *Ea* value decreases by 61% under sunlight irradiation in the temperature range of 150–250 °C, implying that the introduction of light into the thermal catalysis process efficiently reduces the energy barrier that must be surmounted for the methanation reaction to take place. Consequently, the reaction can proceed more rapidly and with a reduced energy input when combining both thermal catalysis and photocatalysis in tandem, showcasing the synergistic interplay between these two catalytic processes. Moreover, the observed *Ea* decline for the light-assisted methanation, as opposed to the in-dark one, together with the linear correlation between the reaction rate and radiant power, indicates that the primary driving force behind the overall methanation reaction mechanism is the photon-induced hot charge carriers. Barrio et al. [71] achieved an E_a of 5.06 kJ mol^{-1} for temperatures between 50 and 200 °C using the Ni (25)/g-CN photocatalyst, which is very close (~26% lower) to the one found in this study. The low E_a value can be attributed to the photocatalytic effect and the hybrid material's adsorption capabilities.

The CH_4 yield was significantly enhanced after incorporating light, with the highest synergy obtained at 150 °C, indicating that the catalysts' intrinsic excitation process may be crucial for the hydrogenation

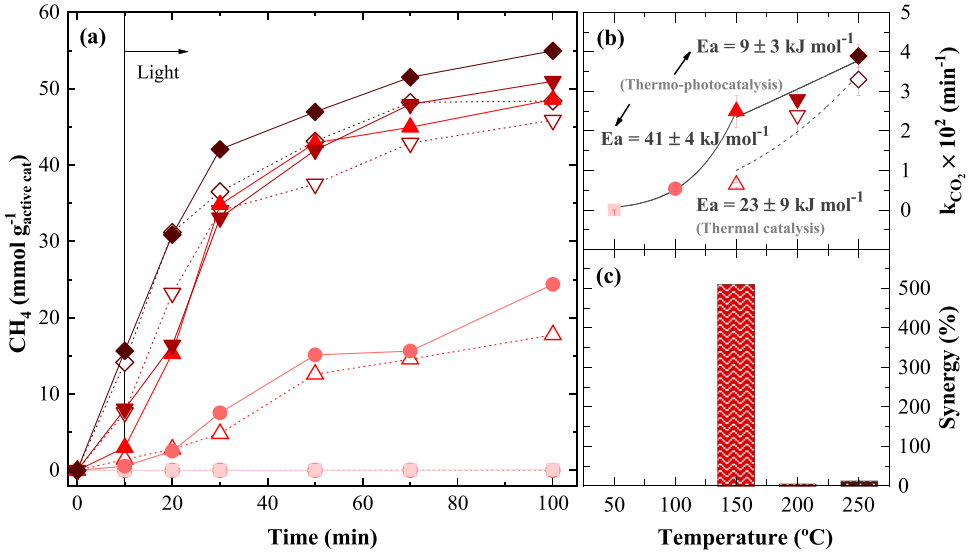

Fig. 9. Representation of (a) specific CH_4 production over time and (b) pseudo-first-order kinetic constants for CO_2 reduction (symbols), along with Arrhenius equation fitting curves (lines) and respective apparent activation energy (Ea) values, for thermal catalysis (open symbols) and solar-assisted thermo-photocatalysis (solid symbols) at different temperatures: 50 °C (■, □); 100 °C (●, ○); 150 °C (▲, △); 200 °C (▼, ▽); and 250 °C (◆, ◇). (c) Synergy of the thermo-photocatalytic methanation process for each temperature. Operating conditions: V = 40 mL; P_{CO2} = 0.32 bar; P_{H2} = 1.28; 30 mg of $RuO_{2(4.0\%)}$:$TiO_{2(26.3\%)}$/Z13X composite; and RP = 0.75 ± 0.01 W (when simulated sunlight was applied).

reaction [13]. At 100 ºC and 150 ºC, there was a substantial increase in CO_2 conversion by approximately 41% and 55%, respectively. Although the adsorption capacities were higher at lower temperatures, CO_2 conversion remained relatively low below 50 ºC. At temperatures above 150 ºC, the adsorption capacity may be reduced; however, higher temperatures may compensate for this catalytic process [66]. Therefore, it can be hypothesised that the heat input and photogenerated carriers supported the CO_2 hydrogenation of CH_4 over the hybrid material. The effect of temperature on the adsorption process is explored in more detail in Section 3.3, focusing on the zeolite 13X adsorbent, $RuO_{2(13.4\%)}$:TiO_2 photocatalyst, and bifunctional $RuO_{2(4.0\%)}$:$TiO_{2(26.3\%)}$/Z13X material.

3.2.5. *Effect of bifunctional material reuse*

The stability of the hybrid $RuO_{2(4.0\%)}$:$TiO_{2(26.3\%)}$/Z13X material towards CO_2 hydrogenation (30 mg, 0.75 W of sunlight radiant power) was evaluated throughout three thermo-photocatalytic consecutive cycles at 150, 200 and 250 ºC (Fig. 10a, Table S5 experiments #6.1 to #6.9). It was inferred that the material's reusability improved at higher temperatures. Upon recycling at 150 and 200 ºC, the CO_2 conversion after 100 min was impaired by 34% and 17%, and the reaction rate decreased by about 69% and 24%, respectively (Fig. 10a.1-a.2, Table S5 experiments and #6.1 to #6.6). In turn, at 250 ºC, the photocatalytic activity was not affected after successive cycles, with the initial CO_2 reaction rate ranging between (0.52 ± 0.04) and (0.62 ± 0.05) mM min^{-1} (Fig. 10a.3, Table S5 experiments #6.7 to #6.9). Although zeolite 13X exhibits a lower adsorption affinity for water, a by-product of the Sabatier reaction, than other zeolite materials [17], it still delivers a higher capability to capture water than CO_2 [72,73], which diminishes as the temperature rises. So, the decrease in the bifunctional photocatalyst/adsorbent composite performance, particularly at lower temperatures, can be attributed to water accumulation (as confirmed by the analyses described below) during consecutive methanation reactions.

To assess any functional changes on the hybrid $RuO_{2(4.0\%)}$:$TiO_{2(26.3\%)}$/Z13X material surface during the reaction, it was analysed by FTIR before and after undergoing three thermo-photocatalytic cycles at temperatures of 150, 200, and 250 ºC (Fig. 10b). The FTIR spectra revealed a peak at 2934 cm^{-1}, corresponding to the C-H stretching vibration of adsorbed hydrocarbons [74], which was attenuated in the

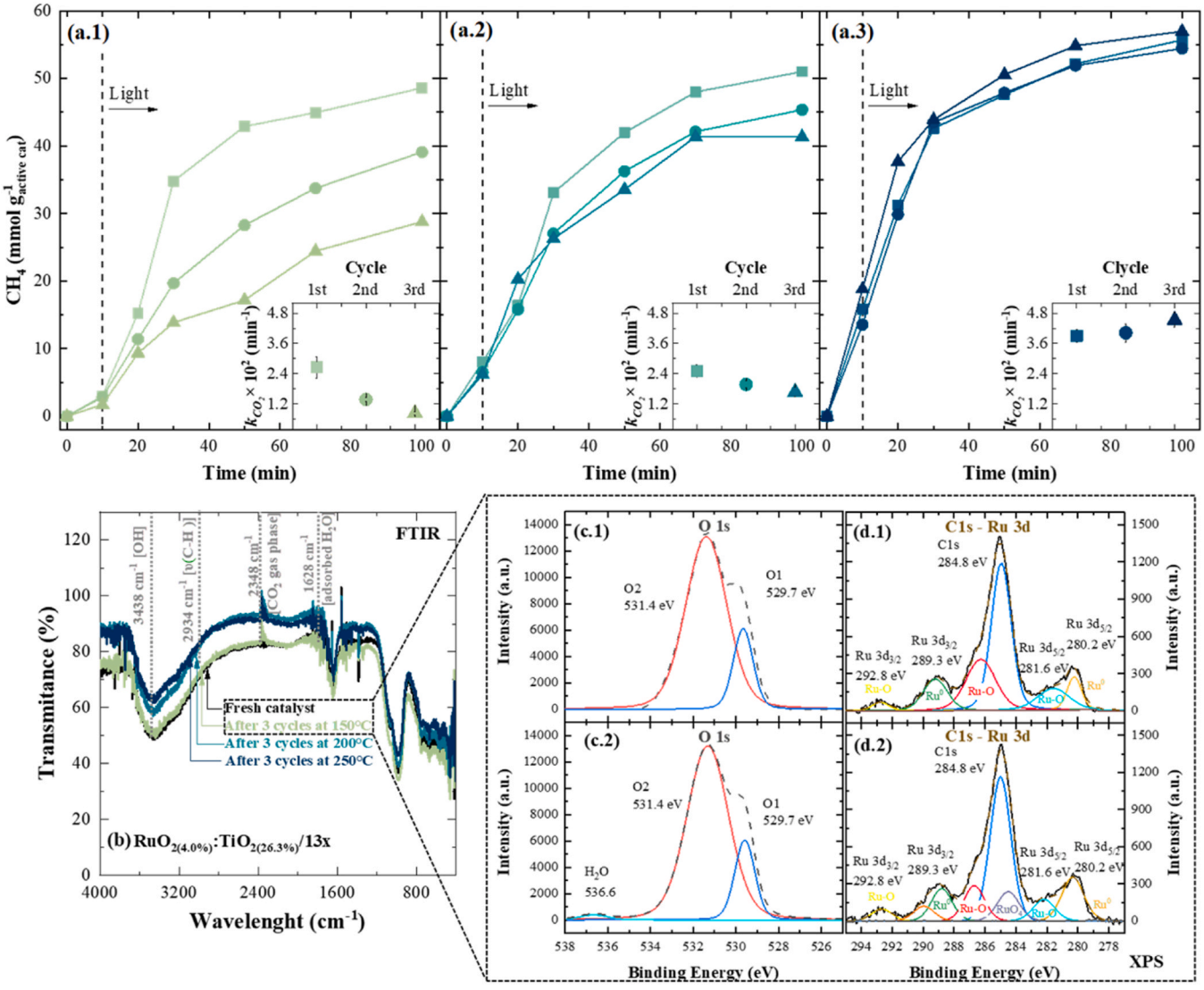

Fig. 10. Representation of: (a) specific CH_4 production over time via solar-assisted thermo-photocatalysis along three sequential reutilization cycles (1 st cycle-■, 2nd cycle-●, and 3rd cycle-▲), and respective pseudo-first-order kinetic constant for CO_2 reduction (inset) at (.1) 150, (.2) 200, and (.3) 250 ºC; (b) FTIR spectra for the fresh $RuO_{2(4.0\%)}$:$TiO_{2(26.3\%)}$/Z13X and after the 3rd utilization cycle at 150, 200, and 250 ºC; and (c-d) high-resolution XPS spectra of the (c) O 1 s and (d) Ti 2p – Ru 3p occupied states (with the respective fitting and deconvolution curves) for the (.1) fresh $RuO_{2(4.0\%)}$:$TiO_{2(26.3\%)}$/Z13X and (.2) after the 3rd utilization cycle at 150 ºC. Operating conditions: V = 40 mL; P_{CO2} = 0.32 bar; P_{H2} = 1.28; 30 mg of $RuO_{2(4.0\%)}$:$TiO_{2(26.3\%)}$/Z13X composite; and RP = 0.75 ± 0.01 W.

sample subjected to the highest temperature. This trend agrees with the fact that higher temperatures lead to higher desorption rates. Furthermore, the presence of water molecules adsorbed on the zeolite-base material is evident, as indicated by the H-OH bending vibration peak at 1628 cm^{-1} and the enhanced OH band at 3438 cm^{-1} [75]. Water deposition onto the porous zeolite increased the intensity of the 1628 cm^{-1} peak in the bifunctional material after three methanation cycles at 150 ºC. Additionally, gas-phase CO_2 adsorption can be observed by the effect at 2348 cm^{-1} [74], which is more pronounced for the reutilised samples than for the fresh ones.

To further investigate the impact of water accumulation on the CO_2 hydrogenation reaction, XPS analysis was performed on the sample that underwent three thermo-photocatalytic cycles at 150 ºC (Fig. 10c-d), as this condition resulted in the least favourable outcomes. Consistent with the findings from the FTIR analysis, the existence of water resulting from the methanation reaction was confirmed by the peak at 536.6 eV in the O 1 s spectra (Fig. 10c.2) [76,77]. This indicates the water adsorption on the recycled hybrid material, whose presence can influence the Ru oxidation state, as evidenced by the formation of the RuO_4 at 284.5 eV in Fig. 10d.2, which can be attributed to double-hydrated RuO_2 [78]. The RuO_4 species can potentially hinder the Sabatier reaction mechanism, as the oxidation and reduction of Ru play crucial roles in the capture and methanation phases, respectively [79]. Moreover, the water adsorbed on the bifunctional material occupies active states, which can compromise the overall effectiveness of the reaction during the subsequent reuse [73].

Therefore, the accumulation of water in the hybrid $RuO_{2(4.0\%)}$:$TiO_{2(26.3\%)}$/Z13X material during a reaction cycle can affect: (i) material's adsorption capacity due to the competition between the CO_2 reactant and H_2O by-product, which has a higher affinity for the available adsorption sites of zeolite 13X; and (ii) the Ru oxidation state due to the double hydration of RuO_2, which results in the formation of RuO_4 species, that negatively impacts the CO_2 methanation reaction. As the temperature rose from 150 to 200ºC, this adverse effect diminished until it became null when the bifunctional material was recycled at 250 ºC. However, the thermal catalysis process predominantly governs the methanation reaction at temperatures higher than 150 ºC. In this sense, other adsorbents, such as zeolite 3 A and zeolite 4 A, can be added to the hybrid material composition to reduce the impact of water accumulation on zeolite 13X at lower temperatures [80,81]. Therefore, it is suitable to foster CO_2 methanation via thermo-photocatalysis, thus levering solar energy to reduce the external heating demand. Furthermore, adding zeolites with enhanced water adsorption capacity will keep water outside the gaseous reactional medium, shifting the Sabatier reaction equilibrium towards the products' side, thus improving the efficiency of the CO_2 hydrogenation into CH_4 at lower temperatures.

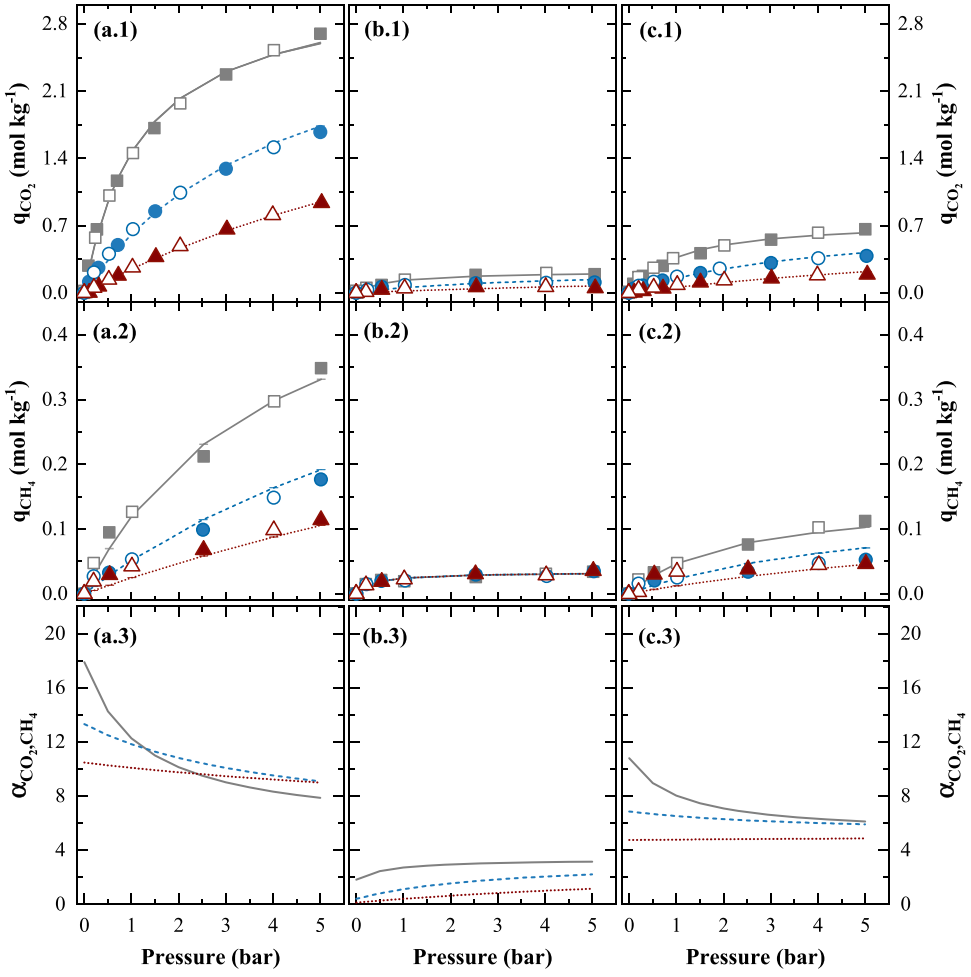

Fig. 11. Adsorption equilibrium isotherms (experimental adsorption (closed symbols) and desorption (open symbols) data along with Lagmuir model fitting lines) for (.1) CO_2 and (.2) CH_4 over the (a) zeolite 13X, (b) $RuO_{2(13.4\%)}$:TiO_2, and (c) $RuO_{2(4.0\%)}$:$TiO_{2(26.3\%)}$/Z13X materials at 150 (■, □, solid lines), 200 (●, ○, dashed lines) and 250 (▲, △, dotted lines) ºC, and (.3) respective selectivity of an equimolar binary CO_2/CH_4 mixture ($\alpha_{CO2,CH4}$).

3.3. Adsorption equilibrium isotherms of the materials

The bifunctional $RuO_{2(4.0\%)}$:$TiO_{2(26.3\%)}$/Z13X material consists of a mixture of $RuO_{2(13.4\%)}$:TiO_2 photocatalyst and zeolite 13X adsorbent. To gain a deeper understanding of the adsorption behaviour and the interaction between the various materials, the equilibrium adsorption-desorption isotherms of CO_2 and CH_4 were examined at temperatures of 150, 200, and 250 °C (temperature range in which methanation can take place via both thermal catalysis and thermo-photocatalysis) under pressures of up to 5 bar. Moreover, the Langmuir model [82] fits the experimental data well, providing valuable insights into the adsorption characteristics and the interaction between the different materials. The results are illustrated in Fig. 11, and the corresponding equilibrium parameters are summarised in Table 1 (calculation formulas are available in the Supplementary Material).

The maximum adsorption capacity (q_m) of CO_2, which is 3.228, 0.223, and 0.7575 mol kg^{-1}, surpasses the q_m of CH_4, which is 0.594, 0.067, and 0.147 mol kg^{-1}, on the zeolite 13X, $RuO_{2(13.4\%)}$:TiO_2, and $RuO_{2(4.0\%)}$:$TiO_{2(26.3\%)}$/Z13X materials, respectively (Table 1). This advantage holds across all temperature and pressure conditions, as illustrated in Fig. 11, providing a clear indication of the benefits of thermo-photocatalysis for the methanation reaction. The strong adsorption affinity of the CO_2 reactant allows it to be preferentially captured and retained on the material surface rather than on the CH_4 product, enhancing the polarisation of CO_2 molecules available for the reaction [83]. The preferential adsorption of CO_2 ensures that it reacts efficiently with H_2 to produce CH_4 on the photocatalyst surface, followed by light product desorption [84].

The amount of CO_2 adsorbed on zeolite 13X agrees with the literature values [85]. According to Campo et al. [86], the equilibrium isotherms of CO_2/CH_4 adsorption on zeolite 13X at 308 K, 323 K, and 348 K using the Langmuir model revealed a q_m value of 7.06/5.30 mol kg^{-1} and the adsorption equilibrium constant at infinite temperature (b_0) of 4.79×10^{-5}/1.41×10^{-4} bar^{-1}. In the present study (Table 1), the CO_2/CH_4 adsorption on the same material exhibited a q_m value of 3.228/0.594 mol kg^{-1}, accompanied by a b_0 value of 4.97×10^{-6} bar^{-1}/2.50×10^{-5} at temperatures of 423, 473, and 523 K. A comparison of the equilibrium isotherms of CO_2/CH_4 adsorption from the current with the reference data revealed that the q_m values decreased 2.2/8.9-fold and b_0 values 9.6/5.6-fold due to the temperature range used. As expected, the $RuO_{2(13.4\%)}$:TiO_2 photocatalyst exhibited the lowest adsorption capacity with q_m for CO_2 of the 0.223 mol kg^{-1} and b_0 value of 9.91×10^{-7}. Adding zeolite 13X to the photocatalyst increased its q_m and b_0 by 3.4- and 2.6-fold, respectively, for CO_2 adsorption (q_m = 0.757 mol kg^{-1} and $b_0 = 2.53 \times 10^{-6}$) (Table 1).

Based on the Langmuir adsorption isotherms and the operating conditions for the CO_2 methanation reaction, it can be estimated that when the photoreactor (40 mL), containing 30 mg of material, is fed with an H_2/CO_2 mixture (4:1) up to a total pressure of 1.6 bar at 20 °C, the bifunctional $RuO_{2(4.0\%)}$:$TiO_{2(26.3\%)}$/Z13X material can adsorb approximately 4.3% of the initial CO_2 concentration (~13 mM), in contrast to the 1.3% capacity of the $RuO_{2(13.4\%)}$:TiO_2 photocatalyst (0.75 *vs* 0.22 mol CO_2 kg^{-1}). When the photoreactor was heated up to 150 °C, its pressure rose to 2.3 bar, resulting in a partial CO_2 pressure of 0.46 bar. Under these conditions, replacing the $RuO_{2(13.4\%)}$:TiO_2 photocatalyst with the hybrid $RuO_{2(4.0\%)}$:$TiO_{2(26.3\%)}$/Z13X material led to a 2.6-fold improvement in CO_2 uptake, from 0.088 to 0.23 mol kg^{-1}, respectively. In fact, these 3.3-/2.6-fold increments in the material adsorption capacity were aligned with a 3.2-fold improvement in the specific CH_4 production rate per mass of active catalyst during thermo-photocatalytic CO_2 hydrogenation (see Table S5, experiments #1.5 and #2.7). Such performance reinforces the advantage of incorporating an adsorbent and a photocatalyst in a single bifunctional material to foster thermo-photocatalytic methanation while reducing the amount of expensive catalyst material required. This innovative approach holds promising potential as a viable and sustainable pathway for solar fuel production.

Under the initial methanation reaction conditions (150 °C; 2.3 bar; [H_2]:[CO_2] = 4:1), pristine zeolite 13X demonstrated an adsorption capacity of 0.89 mol_{CO2} kg^{-1}. If CO_2 partial pressure is increased to 1.67 bar, CO_2 uptake capability rises to 1.88 mol kg^{-1}, which is about 24% higher than the value reported by Silva et al. [87] for binderless beads of zeolite 13X at 1.67 atm (1.69 bar) and 423 K (150 °C). Comparing zeolite 13X with the hybrid material, a 74% decrease in the CO_2 adsorption capacity was observed, in agreement with the 71% reduction in the micropore area (see Table S4). It is important to note that the adsorption ability is not directly proportional to the zeolite 13X content in the bifunctional material due to the physical blocking of zeolite pores by the photocatalyst [30], as previously mentioned in the physical characterisation section (Section 3.1.2). Despite the reduction in adsorption efficiency compared to pure zeolite 13X, the hybrid material still offers the advantages of combined adsorption and catalyst-driven methanation. The conversion of CO_2-to-CH_4 results in the liberation of active spaces within the bifunctional material, further contributing to its utility in CO_2 utilisation processes.

The evaluation of the equimolar CO_2/CH_4 mixture selectivity (calculation formula is available in the Supplementary Material) confirmed that the materials have a higher affinity for CO_2 than CH_4 (Fig. 11a-c.3). The ideal selectivity of both zeolite 13X and photocatalyst/Z13X materials for a binary CO_2/CH_4 mixture demonstrated an inverse relationship with pressure, with a gradual decrease as the pressure rises from 0.1 to 5 bar for all the temperatures tested. In contrast, the photocatalyst exhibited an opposite profile. Considering a temperature of 150 °C (423 K), where the highest synergy between photo- and thermo-catalytic methanation was found, pure zeolite 13X and the hybrid material showed a selectivity decreasing from 16.9 to 7.86 and 10.3–6.12, respectively. In contrast, the photocatalyst's selectivity increases from 2.00 to 3.15 within the same pressure range (0.1–5 bar). Cavenati et al. [88] found a selectivity of 4–6 at the pressure of 0.1–3 bar for CO_2/CH_4 separation using Cu-MOFs adsorbent at 303, 323, 373 K (6.6 mol kg^{-1} at 2.5 bar and 303 K). Silva et al. [87] obtained similar findings, revealing experimental selectivity values of 5.4, 5.5, and 7.4 in an equimolar mixture of CO_2/CH_4 (50/50) at a temperature of 423 K with the respective partial pressure of CO_2/ CH_4 of the 1.67/1.67, 1.00/1.00, and 0.33/0.33 when utilizing binderless beads of zeolite 13X.

Like in catalytic reactions, temperature exerts a considerable influence in adsorption, as depicted in Fig. 11. As the temperature rose, the adsorption capacity decreased for all materials and gases studied. When considering the thermo-photocatalytic system with 30 mg of hybrid material, increasing the temperature from 150 to 250 °C resulted in a 6.8-fold decrease in CO_2 uptake, reducing it from 6.97 to 1.02 μmol (0.23–0.034 mol CO_2 kg^{-1}). This corresponds to 1.34% and 0.20% of the CO_2 initially fed into the reactor. Within this temperature range, the initial CO_2 reduction rate rises from 0.059 ± 0.008–0.45 ±

Table 1
Parameters of the Langmuir model fitting for CO_2 and CH_4 at 423, 473, and 523 K.

Element	Material	q_m^a	b_0^b	$-\Delta H^c$
		mol kg^{-1}	bar^{-1}	kJ mol^{-1}
CO_2	Zeolite 13X	3.228	4.97×10^{-6}	42295
	$RuO_{2(13.4\%)}$:TiO_2	0.223	9.91×10^{-7}	49870
	$RuO_{2(4.0\%)}$:$TiO_{2(26.3\%)}$/Z13X	0.757	2.53×10^{-6}	45193
CH_4	Zeolite 13X	0.594	2.50×10^{-5}	32410
	$RuO_{2(13.4\%)}$:TiO_2	0.067	2.62×10^{-0}	-
	$RuO_{2(4.0\%)}$:$TiO_{2(26.3\%)}$/Z13X	0.147	8.86×10^{-5}	30076

[a] q_m is the maximum adsorption capacity of adsorbent;
[b] b_0 is the adsorption equilibrium constant at an infinite temperature;
[c] ΔH is the heat of adsorption.

0.06 mM min^{-1} for thermal catalysis (TC, heating without light) and from 0.36 ± 0.07–0.51 ± 0.04 mM min^{-1} for thermo-photocatalysis (TPC, heating with light) processes (Table S5, experiments #5.3 - #5.5, and #2.7 - #5.9). In the absence of external heating (reaction at 50 ºC, which is the temperature achieved inside the Suntest's chamber), applying the photocatalysis (PC) process results in an initial CO_2 hydrogenation rate of (0.21 ± 0.03) × 10^{-3} mM min^{-1}. These methanation performances show a decrease in the synergy ($r_{TPC}/(r_{PC} + r_{TC}) - 1$, %) between thermo- and photo-catalysis from 508% to 13.3% while increasing the temperature from 150 to 250 ºC. Indeed, the observed behaviour is consistent with the adsorption profile, where lower CO_2 adsorption on the material surface corresponds to a diminished contribution of photocatalysis to the overall thermo-photocatalytic methanation reaction. Consequently, the likelihood of CO_2 reacting with photogenerated electrons decreases, leading to a more pronounced thermal effect. Such phenomenon highlights the crucial role of adsorption in regulating the interplay between thermal and photocatalytic processes towards the methanation reaction under near-mild conditions. Hence, according to the conversion and adsorption experimental values presented here, thermal photocatalysis is an excellent approach for achieving high CO_2 methanation reaction yields under specific operating conditions that favour the adsorption process over novel bifunctional material. In particular, a temperature of 150 ºC resulted in the highest reaction synergy between adsorption, thermal catalysis, and photocatalysis processes.

4. Conclusions

A highly efficient Ru:TiO_2 photocatalyst-decorated zeolite 13X material has been effectively applied to promote simultaneous adsorption and solar thermo-photocatalytic conversion of CO_2 into renewable CH_4 at 150 ºC. The most significant conclusions were:

(i) Both optimal photocatalyst compositions, $RuO_{2(13.4\%)}$:TiO_2 and $RuO_{2(21.4\%)}$:$SrTiO_3$, exhibited a similar 81% CO_2 conversion after 100 min at 150ºC and 0.75 W; however, the TiO_2-based photocatalyst required a lower amount of noble Ru metal, highlighting its potential as a more cost-effective option for solar thermo-photocatalytic CO_2 methanation.

(ii) The novel bifunctional $RuO_{2(4.0\%)}$:$TiO_{2(26.3\%)}$/Z13X material, which combines the adsorbent and photocatalyst properties, demonstrated excellent performance towards simultaneous CO_2 adsorption/thermo-photoconversion (150ºC and 0.75 W) when prepared by solid-state impregnation. It achieved a specific CH_4 yield rate of 29.2 mmol $g^{-1}_{active\_cat}$ h^{-1} or 309 mmol g^{-1}_{Ru} h^{-1}. Such an outcome denotes that the active catalyst (RuO_2:TiO_2) amount can be reduced by up to 3.3-fold while maintaining a high 88% CO_2 conversion.

(iii) The proposed hybrid material features remarkable versatility in terms of the light source used, achieving high thermo-photocatalytic activities for CO_2 methanation with both 365 and 405 nm LEDs, as well as direct sunlight, which is an advantage regarding practical applications. Notwithstanding, renewable sunlight provided the best balance between CO_2 conversion (88%) and apparent photonic efficiency (15.6%) at a radiant power of 0.75 W.

(iv) The highest synergy between thermal catalysis (dark conditions), photocatalysis (light conditions) was attained at 150 ºC. No CH_4 was detected under dark conditions at lower temperatures, while a low CH_4 production was observed at 50ºC under sunlight, underlining the photochemical reactions' significance. At higher temperatures, similar methanation performances were found for thermal catalysis and thermo-photocatalysis, indicating that solar photons did not significantly contribute to the reaction mechanism.

(v) The accumulation of water, a Sabatier reaction by-product, on the bifunctional material surface impaired its reusability along three consecutive cycles for temperatures below 250 ºC. This is due to the higher adsorption affinity of water for zeolite 13X compared to CO_2 and the resulting change in the Ru oxidation state by the RuO_2 double-hydration.

(vi) The experimental adsorption equilibrium isotherms displayed a higher CO_2 adsorption capacity at lower temperatures, consistent with the thermo-photocatalytic test results. The superior adsorption capacity of CO_2 compared to CH_4 in hybrid material confers a distinct advantage towards photocatalytic methanation. The bifunctional material's adsorption was about 2.6-fold higher than the photocatalyst, favoring CH_4 production per mass of active photocatalyst. The high yield of CO_2 methanation at 150 ºC can be attributed to the simultaneous contribution of adsorption and thermo-photocatalytic processes.

This work highlights the importance of carefully optimizing the operating conditions to maximize the efficiency of the methanation reaction and underscores the potential of adsorption/thermo-photocatalysis as a promising method for CO_2 conversion to methane.

CRediT authorship contribution statement

Rui A.R. Boaventura: Funding acquisition, Supervision, Writing – review & editing. **Vítor J.P. Vilar:** Conceptualization, Funding acquisition, Supervision, Writing – review & editing. **Tânia F.C.V.Silva:** Conceptualization, Funding acquisition, Project administration, Supervision, Visualization, Writing – review & editing. **Larissa O. Paulista:** Formal analysis, Investigation, Validation, Visualization, Writing – original draft. **Alexandre F.P. Ferreira:** Conceptualization, Funding acquisition, Supervision, Writing – review & editing. **Alírio E. Rodrigues:** Funding acquisition, Writing – review & editing. **Ramiro J.E. Martins:** Funding acquisition, Supervision, Writing – review & editing.

Declaration of Competing Interest

The authors declare that they have no known competing financial interests or personal relationships that could have appeared to influence the work reported in this paper.

Data Availability

The authors are unable or have chosen not to specify which data has been used.

Acknowledgments

This work was supported by sources provided by: (i) national funds through *Fundação para a Ciência e a Tecnologia* (FCT), and *Ministério da Ciência, Tecnologia e Ensino Superior* (MCTES), Portugal, in the framework of *Programa de Investimento e Despesas de Desenvolvimento da Administração Central* (PIDDAC), under Project CO2-to-CH4, 2022.01176.PTDC (DOI: 10.54499/2022.01176.PTDC); and (ii) Norte Portugal Regional Operational Programme (NORTE 2020), in the framework of the PORTUGAL 2020 Partnership Agreement, through the European Regional Development Fund (ERDF), under the project HyGreen&LowEmissions, NORTE-01–0145-FEDER-000077. This research was also funded by (iii) FCT/MCTES (PIDDAC): LSRE-LCM - UIDB/50020/2020 (DOI: 10.54499/UIDB/50020/2020) and UIDP/50020/2020 (DOI: 10.54499/UIDP/50020/2020); and ALiCE - LA/P/0045/2020 (DOI: 10.54499/LA/P/0045/2020). Larissa O. Paulista acknowledges the Ph.D. fellowship supported by FCT (reference SFRH/BD/137639/2018 and COVID/BD/152922/2022). Vítor J.P. Vilar and Tânia F.C.V. Silva acknowledges the FCT Individual Call to Scientific Employment Stimulus 2017 (CEECIND/01317/2017 and CEECIND/01386/2017).

Appendix A. Supporting information

Supplementary data associated with this article can be found in the online version at doi:10.1016/j.jece.2024.112418.

References

[1] Intergovernmental Panel on Climate Change (IPCC), Climate Change 2022: Impacts, Adaptation and Vulnerability, in, 2022.

[2] W. Tu, Y. Zhou, Z. Zou, Photocatalytic conversion of CO_2 into renewable hydrocarbon fuels: state-of-the-art accomplishment, challenges, and prospects, Adv. Mater. 26 (2014) 4607–4626, https://doi.org/10.1002/adma.201400087.

[3] S.L. Wong, B.B. Nyakuma, A.H. Nordin, C.T. Lee, N. Ngadi, K.Y. Wong, O. Oladokun, Uncovering the dynamics in global carbon dioxide utilization research: a bibliometric analysis (1995–2019), Environ. Sci. Pollut. Res. 28 (2021) 13842–13860, https://doi.org/10.1007/s11356-020-11643-w.

[4] W.D. Jones, Carbon capture and conversion, J. Am. Chem. Soc. 142 (2020) 4955–4957, https://doi.org/10.1021/jacs.0c02356.

[5] A. Bijanzadeh, M. Vakili, R. Khordad, A study of the surface plasmon absorption band for nanoparticles, Int. J. Phys. Sci. 7 (2012) 1943–1948, https://doi.org/10.5897/IJPS11.893.

[6] R. Marschall, L. Wang, Non-metal doping of transition metal oxides for visible-light photocatalysis, Catal. Today 225 (2014) 111–135, https://doi.org/10.1016/j.cattod.2013.10.088.

[7] X. Huang, J. Wang, T. Li, J. Wang, M. Xu, W. Yu, A. El Abed, X. Zhang, Review on optofluidic microreactors for artificial photosynthesis, Beilstein J. Nanotechnol. 9 (2018) 30–41, https://doi.org/10.3762/bjnano.9.5.

[8] A. Crake, K.C. Christoforidis, A. Kafizas, S. Zafeiratos, C. Petit, CO2 capture and photocatalytic reduction using bifunctional TiO2/MOF nanocomposites under UV–vis irradiation, Appl. Catal. B: Environ. 210 (2017) 131–140, https://doi.org/10.1016/j.apcatb.2017.03.039.

[9] A.-Y. Lo, F. Taghipour, Review and prospects of microporous zeolite catalysts for CO2 photoreduction, Appl. Mater. Today 23 (2021) 101042, https://doi.org/10.1016/j.apmt.2021.101042.

[10] X. Chen, F. Jin, Photocatalytic reduction of carbon dioxide by titanium oxide-based semiconductors to produce fuels, Front. Energy 13 (2019) 207–220, https://doi.org/10.1007/s11708-019-0628-9.

[11] C. Luo, J. Zhao, Y. Li, W. Zhao, Y. Zeng, C. Wang, Photocatalytic CO_2 reduction over $SrTiO_3$: correlation between surface structure and activity, Appl. Surf. Sci. 447 (2018) 627–635, https://doi.org/10.1016/j.apsusc.2018.04.049.

[12] K. Guo, X. Zhu, L. Peng, Y. Fu, R. Ma, X. Lu, F. Zhang, W. Zhu, M. Fan, Boosting photocatalytic CO_2 reduction over a covalent organic framework decorated with ruthenium nanoparticles, Chem. Eng. J. 405 (2021) 127011, https://doi.org/10.1016/j.cej.2020.127011.

[13] B. Jin, X. Ye, H. Zhong, F. Jin, Y.H. Hu, Enhanced photocatalytic CO_2 hydrogenation with wide-spectrum utilization over black TiO_2 supported catalyst, Chin. Chem. Lett. 33 (2022) 812–816, https://doi.org/10.1016/j.cclet.2021.07.046.

[14] D. Mateo, J. Albero, H. García, Titanium-perovskite-supported RuO_2 nanoparticles for photocatalytic CO_2 methanation, Joule 3 (2019) 1949–1962, https://doi.org/10.1016/j.joule.2019.06.001.

[15] G. Singh, J. Lee, A. Karakoti, R. Bahadur, J. Yi, D. Zhao, K. AlBahily, A. Vinu, Emerging trends in porous materials for CO_2 capture and conversion, Chem. Soc. Rev. 49 (2020) 4360–4404, https://doi.org/10.1039/D0CS00075B.

[16] C. Wang, S. Fang, S. Xie, Y. Zheng, Y.H. Hu, Thermo-photo catalytic CO_2 hydrogenation over Ru/TiO_2, J. Mater. Chem. A 8 (2020) 7390–7394, https://doi.org/10.1039/C9TA13275A.

[17] M.C. Bacariza, I. Graça, J.M. Lopes, C. Henriques, Tuning zeolite properties towards CO_2 methanation: An overview, ChemCatChem 11 (2019) 2388–2400, https://doi.org/10.1002/cctc.201900229.

[18] L.O. Paulista, J. Albero, R.J. Martins, R.A. Boaventura, V.J. Vilar, T.F. Silva, H. García, Turning carbon dioxide and ethane into ethanol by solar-driven heterogeneous photocatalysis over RuO_2-and NiO-co-Doped $SrTiO_3$, Catalysts 11 (2021) 461, https://doi.org/10.3390/catal11040461.

[19] L.O. Paulista, A.F.P. Ferreira, B. Castanheira, M.B. Đolić, R.J.E. Martins, R.A. R. Boaventura, V.J.P. Vilar, T.F.C.V. Silva, Solar-driven thermo-photocatalytic CO2 methanation over a structured RuO2:TiO2/SBA-15 nanocomposite at low temperature, Appl. Catal. B: Environ. 340 (2024), https://doi.org/10.1016/j.apcatb.2023.123232.

[20] J.A. Martins, A.C. Faria, M.A. Soria, C.V. Miguel, A.E. Rodrigues, L.M. Madeira, CO_2 methanation over hydrotalcite-derived nickel/ruthenium and supported ruthenium catalysts, Catalysts 9 (2019) 1008, https://doi.org/10.3390/catal9121008.

[21] J. Hong, W. Zhang, J. Ren, R. Xu, Photocatalytic reduction of CO_2: a brief review on product analysis and systematic methods, Anal. Methods 5 (2013) 1086–1097, https://doi.org/10.1039/C2AY26270C.

[22] M. Horn, C. Schwebdtfeger, E. Meagher, Refinement of the structure of anatase at several temperatures, Z. F. üR. Krist. -Cryst. Mater. 136 (1972) 273–281, https://doi.org/10.1524/zkri.1972.136.16.273.

[23] L. Palliyaguru, U.S. Kulathunga, L.I. Jayarathna, C.D. Jayaweera, P.M. Jayaweera, A simple and novel synthetic route to prepare anatase TiO_2 nanopowders from natural ilmenite via the H_3PO_4/NH_3 process, Int. J. Miner., Metall. Mater. 27 (2020) 846–855, https://doi.org/10.1007/s12613-020-2030-3.

[24] A.A. Bolzan, C. Fong, B.J. Kennedy, C.J. Howard, Structural studies of rutile-type metal dioxides, Acta Crystallogr. Sect. B: Struct. Sci. 53 (1997) 373–380, https://doi.org/10.1107/S0108768197001468.

[25] G. Calestani, G. Bacca, G. Andreetti, Structural study of zeolite X exchanged with 'f' transition elements. I. Crystal structure of reference hydrated Na X, Zeolites 7 (1987) 54–58, https://doi.org/10.1016/0144-2449(87)90120-5.

[26] J.I. Goldstein, D.E. Newbury, J.R. Michael, N.W. Ritchie, J.H.J. Scott, D.C. Joy, Scanning electron microscopy and X-ray microanalysis, Springer, 2017.

[27] E. Alrin, C.R. Tjampakasari, Y.K. Krisnandi, Metal-organic framework derived ZnO/porous carbon – 13X zeolite composite modified with chitosan and silver nanoparticles as versatile antibacterial agent, Inorg. Chem. Commun. 144 (2022) 109943, https://doi.org/10.1016/j.inoche.2022.109943.

[28] V. Tejavath, V. Kasarabada, S. Gonuguntla, V. Perupoga, S.V. Nandury, S. Bojja, U. Pal, Technoeconomic investigation of amine-grafted zeolites and their kinetics for CO_2 capture, ACS Omega 6 (2021) 6153–6162, https://doi.org/10.1021/acsomega.0c05397.

[29] Z.A. ALOthman, A review: fundamental aspects of silicate mesoporous materials, Mater. (Basel) 5 (2012) 2874–2902, https://doi.org/10.3390%2Fma5122874.

[30] F. Gramigni, U. Iacobone, N.D. Nasello, T. Selleri, N. Usberti, I. Nova, Review of hydrocarbon poisoning and deactivation effects on Cu-Zeolite, Fe-Zeolite, and vanadium-based selective catalytic reduction catalysts for NOx removal from lean exhausts, Ind. Eng. Chem. Res. 60 (2021) 6403–6420, https://doi.org/10.1021/acs.iecr.0c05894.

[31] C. Zhou, A. Alshameri, C. Yan, X. Qiu, H. Wang, Y. Ma, Characteristics and evaluation of synthetic 13X zeolite from Yunnan's natural halloysite, J. Porous Mater. 20 (2013) 587–594, https://doi.org/10.1007/s10934-012-9631-9.

[32] S. Linic, P. Christopher, D.B. Ingram, Plasmonic-metal nanostructures for efficient conversion of solar to chemical energy, Nat. Mater. 10 (2011) 911–921, https://doi.org/10.1038/nmat3151.

[33] M.T. Uddin, Y. Nicolas, C. Olivier, T. Toupance, M.M. Müller, H.-J. Kleebe, K. Rachut, J. Ziegler, A. Klein, W. Jaegermann, Preparation of RuO_2/TiO_2 mesoporous heterostructures and rationalization of their enhanced photocatalytic properties by band alignment investigations, J. Phys. Chem. C. 117 (2013) 22098–22110, https://doi.org/10.1021/jp407539c.

[34] S. Sasikala, K.H. Gopi, S.D. Bhat, Sulfosuccinic acid-sulfonated polyether ether ketone/organo functionalized microporous zeolite-13X membrane electrolyte for direct methanol fuel cells, Microporous Mesoporous Mater. 236 (2016) 38–47, https://doi.org/10.1016/j.micromeso.2016.08.029.

[35] R. Vinodh, C. Deviprasath, C.V.M. Gopi, V.G.R. Kummara, R. Atchudan, T. Ahamad, H.-J. Kim, M. Yi, Novel 13X Zeolite/PANI electrocatalyst for hydrogen and oxygen evolution reaction, Int. J. Hydrog. Energy 45 (2020) 28337–28349, https://doi.org/10.1016/j.ijhydene.2020.07.194.

[36] Y. Li, W. Wei, J. Chen, L. Zu, Y. Zhou, J. Wu, X. Wu, Atomic layer deposition precisely modified zeolite 13X: Physicochemical synergistic adsorption of space molecular contaminants, Appl. Surf. Sci. 590 (2022) 153084, https://doi.org/10.1016/j.apsusc.2022.153084.

[37] W. Lu, Y. Iwasa, Y. Ou, D. Jinno, S. Kamiyama, P.M. Petersen, H. Ou, Effective optimization of surface passivation on porous silicon carbide using atomic layer deposited Al_2O_3, Rsc Adv. 7 (2017) 8090–8097, https://doi.org/10.1039/C6RA27281A.

[38] XPS, The International XPS Database, in, 2022.

[39] H. Wang, X. Li, Q. Ruan, J. Tang, Ru and RuO x decorated carbon nitride for efficient ammonia photosynthesis, Nanoscale 12 (2020) 12329–12335, https://doi.org/10.1039/D0NR02527E.

[40] K. Zhang, Q. Meng, H. Wu, T. Yuan, S. Han, J. Zhai, B. Zheng, C. Xu, W. Wu, M. He, Levulinic acid hydrogenation to γ-valerolactone over single Ru atoms on a TiO_2 @nitrogen doped carbon support, Green. Chem. 23 (2021) 1621–1627, https://doi.org/10.1039/D0GC04108D.

[41] A.S. Asundi, A.S. Hoffman, S.S. Nathan, A. Boubnov, S.R. Bare, S.F. Bent, Impurity control in catalyst design: the role of sodium in promoting and stabilizing Co and Co_2C for syngas conversion 13 (2021) 1186–1194, https://doi.org/10.1002/cctc.202001703.

[42] S.C. Erwin, L. Zu, M.I. Haftel, A.L. Efros, T.A. Kennedy, D.J. Norris, Doping semiconductor nanocrystals, Nature 436 (2005) 91–94, https://doi.org/10.1038/nature03832.

[43] Y. Sun, T. Hu, W. Zhang, X. Chen, Photocatalytic degradation of phenol on strontium titanate supported on HZSM-5, J. Adv. Oxid. Technol. 20 (2017), https://doi.org/10.1515/jaots-2016-0194.

[44] P. Praveen, G. Viruthagiri, S. Mugundan, N. Shanmugam, Structural, optical and morphological analyses of pristine titanium di-oxide nanoparticles–Synthesized via sol–gel route, Spectrochim. Acta Part A: Mol. Biomol. Spectrosc. 117 (2014) 622–629, https://doi.org/10.1016/j.saa.2013.09.037.

[45] K.-W. Park, Modification of graphene oxide and preparation of RuO_2 nanocomposites, Prepr. Org. (2020), https://doi.org/10.20944/preprints202003.0312.v1.

[46] P. Joshi, D. Sutrave, A comparative study of structural and morphological properties of pristine and Mn doped ruthenium oxide thin films, Int. J. Thin Films Sci. Technol. 6 (2017) 83–86, https://doi.org/10.18576/ijtfst/060206.

[47] R. Viter, I. Iatsunskyi, Optical spectroscopy for characterization of metal oxide nanofibers, Handb. Nanofibers 5 (2018) 1–35, https://doi.org/10.1007/978-3-319-53655-2_10.

[48] M. Ismael, Highly effective ruthenium-doped TiO_2 nanoparticles photocatalyst for visible-light-driven photocatalytic hydrogen production, N. J. Chem. 43 (2019) 9596–9605, https://doi.org/10.1039/C9NJ02226K.

[49] H. Liu, A.Q. Dao, C. Fu, Activities of combined TiO_2 semiconductor nanocatalysts under solar light on the reduction of CO_2, J. Nanosci. Nanotechnol. 16 (2016) 3437–3446, https://doi.org/10.1166/jnn.2016.11854.

[50] T. Xue, K. Osseo-Asare, Heterogeneous equilibria in the Ru-H_2O, Ru-Cl-H_2O and Ru-S-H_2O systems, J. Less Common Met. 152 (1989) 103–114, https://doi.org/10.1016/0022-5088(89)90075-1.

[51] S. Al Jitan, G. Palmisano, C. Garlisi, Synthesis and surface modification of TiO_2-based photocatalysts for the conversion of CO_2, Catalysts 10 (2020) 227, https://doi.org/10.3390/catal10020227.

[52] S. Hashimoto, Zeolite photochemistry: impact of zeolites on photochemistry and feedback from photochemistry to zeolite science, J. Photochem. Photobiol. C: Photochem. Rev. 4 (2003) 19–49, https://doi.org/10.1016/S1389-5567(03)00003-0.

[53] S. Chai, Y. Men, J. Wang, S. Liu, Q. Song, W. An, G. Kolb, Boosting CO_2 methanation activity on Ru/TiO_2 catalysts by exposing (001) facets of anatase TiO_2, J. CO_2 Util. 33 (2019) 242–252, https://doi.org/10.1016/j.jcou.2019.05.031.

[54] Q. Lin, X.Y. Liu, Y. Jiang, Y. Wang, Y. Huang, T.J.C.S. Zhang, Technology, Crystal phase effects on the structure and performance of ruthenium nanoparticles for CO_2 hydrogenation, Catal. Sci. Technol. 4 (2014) 2058–2063, https://doi.org/10.1039/C4CY00030G.

[55] H. Ge, Y. Kuwahara, K. Kusu, Z. Bian, H. Yamashita, Ru/H$xMoO_3$-y with plasmonic effect for boosting photothermal catalytic CO_2 methanation, Appl. Catal. B: Environ. 317 (2022) 121734, https://doi.org/10.1016/j.apcatb.2022.121734.

[56] M. Khalil, J. Gunlazuardi, T.A. Ivandini, A. Umar, Photocatalytic conversion of CO_2 using earth-abundant catalysts: A review on mechanism and catalytic performance, Renew. Sustain. Energy Rev. 113 (2019) 109246, https://doi.org/10.1016/j.rser.2019.109246.

[57] B.M. da Costa Filho, V.J.P. Vilar, Strategies for the intensification of photocatalytic oxidation processes towards air streams decontamination: a review, Chem. Eng. J. 391 (2020) 123531, https://doi.org/10.1016/j.cej.2019.123531.

[58] A.L. Linsebigler, G. Lu, J.T. Yates Jr, Photocatalysis on TiO_2 surfaces: principles, mechanisms, and selected results, Chem. Rev. 95 (1995) 735–758, https://doi.org/10.1021/cr00035a013.

[59] A. Fujishima, T.N. Rao, D.A. Tryk, Titanium dioxide photocatalysis, J. Photochem. Photobiol. C: Photochem. Rev. 1 (2000) 1–21, https://doi.org/10.1016/S1389-5567(00)00002-2.

[60] S. Sarina, E. Jaatinen, Q. Xiao, Y.M. Huang, P. Christopher, J.C. Zhao, H.Y. Zhu, Photon energy threshold in direct photocatalysis with metal nanoparticles: key evidence from the action spectrum of the reaction, J. Phys. Chem. Lett. 8 (2017) 2526–2534, https://doi.org/10.1021/acs.jpclett.7b00941.

[61] K.L. Wouters, N.R. de Tacconi, R. Konduri, R.O. Lezna, F.M. MacDonnell, Driving multi-electron reactions with photons: Dinuclear ruthenium complexes capable of stepwise and concerted multi-electron reduction, Photosynth. Res. 87 (2006) 41–55, https://doi.org/10.1007/s11120-005-6398-8.

[62] M. Tahir, B. Tahir, Constructing a stable 2D/2D heterojunction of oxygen-cluster-modified Ti_3AlC_2 MAX cocatalyst with proton-rich C_3N_4 for highly efficient photocatalytic CO_2 methanation, Ind. Eng. Chem. Res. 59 (2020) 9841–9857, https://doi.org/10.1021/acs.iecr.0c00193.

[63] S. Sorcar, Y. Hwang, C.A. Grimes, S.-I. In, Highly enhanced and stable activity of defect-induced titania nanoparticles for solar light-driven CO_2 reduction into CH_4, Mater. Today 20 (2017) 507–515, https://doi.org/10.1016/j.mattod.2017.09.005.

[64] W.A. Thompson, E. Sanchez Fernandez, M.M. Maroto-Valer, Review and analysis of CO_2 photoreduction kinetics, ACS Sustain. Chem. Eng. 8 (2020) 4677–4692, https://doi.org/10.1021/acssuschemeng.9b06170.

[65] D. Mateo, J.L. Cerrillo, S. Durini, J. Gascon, Fundamentals and applications of photo-thermal catalysis, hemical Soc. Rev. 50 (2021) 2173–2210, https://doi.org/10.1039/D0CS00357C.

[66] M. Cavallo, M. Dosa, N.G. Porcaro, F. Bonino, M. Piumetti, V. Crocellà, Shaped natural and synthetic zeolites for CO_2 capture in a wide temperature range, J. CO_2 Util. 67 (2023) 102335, https://doi.org/10.1016/j.jcou.2022.102335.

[67] A. Olivo, E. Ghedini, M. Signoretto, M. Compagnoni, I. Rossetti, Liquid vs. gas phase CO_2 photoreduction process: which is the effect of the reaction medium? Energies 10 (2017) 1394, https://doi.org/10.3390/en10091394.

[68] F. Zhang, Y.-H. Li, M.-Y. Qi, Y.M.A. Yamada, M. Anpo, Z.-R. Tang, Y.-J. Xu, Photothermal catalytic CO_2 reduction over nanomaterials, Chem. Catal. (2021), https://doi.org/10.1016/j.checat.2021.01.003.

[69] A. Karelovic, P. Ruiz, Mechanistic study of low temperature CO_2 methanation over Rh/TiO_2 catalysts, J. Catal. 301 (2013) 141–153, https://doi.org/10.1016/j.jcat.2013.02.009.

[70] S. Ullah, E.C. Lovell, T.H. Tan, B. Xie, P.V. Kumar, R. Amal, J. Scott, Photoenhanced CO_2 methanation over La_2O_3 promoted Co/TiO_2 catalysts, Appl. Catal. B: Environ. 294 (2021) 120248, https://doi.org/10.1016/j.apcatb.2021.120248.

[71] J. Barrio, D. Mateo, J. Albero, H. García, M. Shalom, A Heterogeneous carbon nitride–nickel photocatalyst for efficient low-temperature CO_2 methanation, Adv. Energy Mater. 9 (2019) 1902738, https://doi.org/10.1002/aenm.201902738.

[72] G. Li, P. Xiao, P.A. Webley, J. Zhang, R. Singh, Competition of CO_2/H_2O in adsorption based CO_2 capture, Energy Procedia 1 (2009) 1123–1130, https://doi.org/10.1016/j.egypro.2009.01.148.

[73] L. Joos, J.A. Swisher, B. Smit, Molecular simulation study of the competitive adsorption of H_2O and CO_2 in zeolite 13X, Langmuir 29 (2013) 15936–15942, https://doi.org/10.1021/la403824g.

[74] L. Liu, Y. Li, Understanding the reaction mechanism of photocatalytic reduction of CO_2 with H_2O on TiO_2-based photocatalysts: a review, Aerosol air Qual. Res. 14 (2014) 453–469, https://doi.org/10.4209/aaqr.2013.06.0186.

[75] S.M. Amininasab, S. Nouri, Sol-gel synthesis of ionic liquid/zeolite nano-particles as green, reusable adsorbents for removal of nitrate from aqueous solution, J. Sol.-Gel Sci. Technol. (2022) 1–12, https://doi.org/10.1007/s10971-022-05823-y.

[76] C.-T. Dinh, A. Jain, F. de Arquer, P. De Luna, J. Li, N. Wang, X. Zheng, J. Cai, B. Z. Gregory, O. Voznyy, Multi-site electrocatalysts for hydrogen evolution in neutral media by destabilization of water molecules, Nat. Energy 4 (2019) 107–114, https://doi.org/10.1038/s41560-018-0296-8.

[77] H. Ali-Löytty, M.W. Louie, M.R. Singh, L. Li, H.G. Sanchez Casalongue, H. Ogasawara, E.J. Crumlin, Z. Liu, A.T. Bell, A. Nilsson, Ambient-pressure XPS study of a Ni–Fe electrocatalyst for the oxygen evolution reaction, J. Phys. Chem. C. 120 (2016) 2247–2253, https://doi.org/10.1021/acs.jpcc.5b10931.

[78] T. Spătaru, L. Preda, P. Osiceanu, C. Munteanu, M. Marcu, C. Lete, N. Spătaru, A. Fujishima, Electrochemical deposition of Pt–RuO x· nH_2O composites on conductive diamond and its application to methanol oxidation in acidic media, Electrocatalysis 7 (2016) 140–148, https://doi.org/10.1007/s12678-015-0292-8.

[79] S. Wang, R.J. Farrauto, S. Karp, J.H. Jeon, E.T. Schrunk, Parametric, cyclic aging and characterization studies for CO_2 capture from flue gas and catalytic conversion to synthetic natural gas using a dual functional material (DFM), J. CO_2 Util. 27 (2018) 390–397, https://doi.org/10.1016/j.jcou.2018.08.012.

[80] B.A. Santos, V.M. Silva, J.M. Loureiro, A.E. Rodrigues, Adsorption of H_2O and dimethyl carbonate at high pressure over zeolite 3A in fixed bed column, Ind. Eng. Chem. Res. 53 (2014) 2473–2483, https://doi.org/10.1021/ie403830r.

[81] W. Zhu, L. Gora, A.W.C. van den Berg, F. Kapteijn, J.C. Jansen, J.A. Moulijn, Water vapour separation from permanent gases by a zeolite-4A membrane, J. Membr. Sci. 253 (2005) 57–66, https://doi.org/10.1016/j.memsci.2004.12.039.

[82] C. Nguyen, D.D. Do, Dual langmuir kinetic model for adsorption in carbon molecular sieve materials, Langmuir 16 (2000) 1868–1873, https://doi.org/10.1021/la990584m.

[83] N.H. Khdary, A.S. Alayyar, L.M. Alsarhan, S. Alshihri, M. Mokhtar, Metal oxides as catalyst/supporter for CO_2 capture and conversion, Review 12 (2022) 300, https://doi.org/10.3390/catal12030300.

[84] I.S. Omodolor, H.O. Otor, J.A. Andonegui, B.J. Allen, A.C. Alba-Rubio, Dual-function materials for CO_2 capture and conversion: a review, Ind. Eng. Chem. Res. 59 (2020) 17612–17631, https://doi.org/10.1021/acs.iecr.0c02218.

[85] G. Mondino, C.A. Grande, R. Blom, L.O. Nord, Moving bed temperature swing adsorption for CO_2 capture from a natural gas combined cycle power plant, Int. J. Greenh. Gas. Control 85 (2019) 58–70, https://doi.org/10.1016/j.ijggc.2019.03.021.

[86] M.C. Campo, A.M. Ribeiro, A.F.P. Ferreira, J.C. Santos, C. Lutz, J.M. Loureiro, A. E. Rodrigues, Carbon dioxide removal for methane upgrade by a VSA process using an improved 13X zeolite, Fuel Process. Technol. 143 (2016) 185–194, https://doi.org/10.1016/j.fuproc.2015.11.024.

[87] J.A.C. Silva, A.F. Cunha, K. Schumann, A.E. Rodrigues, Binary adsorption of CO_2/CH_4 in binderless beads of 13X zeolite, Microporous Mesoporous Mater. 187 (2014) 100–107, https://doi.org/10.1016/j.micromeso.2013.12.017.

[88] S. Cavenati, C.A. Grande, A.E. Rodrigues, C. Kiener, U. Müller, Metal organic framework adsorbent for biogas upgrading, Ind. Eng. Chem. Res. 47 (2008) 6333–6335, https://doi.org/10.1021/ie8005269.